

Mixed Ligand Mononuclear Copper(II) Complex as a Promising Anticancer Agent: Interaction Studies with DNA/HSA, Molecular Docking, and In Vitro Cytotoxicity Studies

Kumudini Paliwal, Paramita Haldar, P. K. Sudhadevi Antharjanam, and Manjuri Kumar*



Cite This: *ACS Omega* 2022, 7, 21961–21977



Read Online

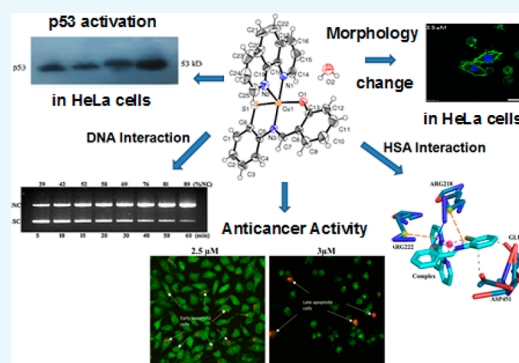
ACCESS |

Metrics & More

Article Recommendations

Supporting Information

ABSTRACT: The isolated copper(II) complex $[\text{CuL}(o\text{-phen})]\cdot\text{H}_2\text{O}$ (**1**) [$\text{H}_2\text{L} = o\text{-HO-C}_6\text{H}_4\text{C}(\text{H})=\text{N-C}_6\text{H}_4\text{-SH-}o$, $o\text{-phen} = 1,10\text{-phenanthroline}$] was structurally characterized using single-crystal X-ray crystallography. **1** in CH_3CN at liquid nitrogen temperature displayed a characteristic monomeric X-band electron paramagnetic resonance spectrum having a tetragonal character with $g_{\parallel} = 2.1479$ and $g_{\perp} = 2.0691$ and $A_{\parallel} \approx 18.0$ mT and $A_{\perp} \leq 3.9$ mT, respectively. **1** showed a strong binding affinity toward calf thymus DNA as reflected from its intrinsic binding constant ($K_b = 7.88 \times 10^5 \text{ M}^{-1}$), and its competitive displacement of ethidium bromide suggested an intercalative DNA-binding mode ($K_{\text{app}} = 1.32 \times 10^6 \text{ M}^{-1}$). This was confirmed from the viscosity study that showed an increase in the viscosity of DNA with an increasing concentration of **1**. Complex **1** is highly efficient in promoting oxidative and hydrolytic DNA cleavage ($k_{\text{obs}} = 1.987 \text{ h}^{-1}$). **1** showed a strong binding affinity with the carrier protein human serum albumin (HSA) ($K_a = 5.22 \times 10^5 \text{ M}^{-1}$). A high bimolecular quenching constant $k_q = 2.29 \times 10^{13} \text{ M}^{-1}\text{s}^{-1}$ indicated a static quenching mechanism involved in the fluorescence quenching of HSA by **1**. Fluorescence resonance energy transfer theory suggested that the distance ($r = 3.52$ nm) between **1** and HSA is very close. Molecular docking studies suggested that **1** primarily binds to HSA in subdomain IIA. A protein–ligand interaction profiler was used to visualize hydrophobic, hydrogen bonds, and π -cation interactions between HSA and **1**. A 3-(4,5-dimethylthiazol-2-yl)-2,5-diphenyltetrazolium bromide assay using HeLa and MDA-MB-231 cells showed a significant in vitro anticancer activity of **1** (IC_{50} 2.63 and 2.68 μM , respectively). Nuclear staining assays suggested apoptotic cell death in HeLa cells treated with **1**. The effect of **1** on the cytoskeletal actin filaments visualized using phalloidin staining showed extensive destruction of actin filaments. Flow cytometric analysis indicated that **1** inhibits the growth of HeLa cells through cell cycle arrest in the S phase. Western blot analysis showed upregulation in the expression of apoptotic marker proteins caspase 3, p53, and Bax. These results collectively indicate that **1** induces apoptosis by promoting DNA damage and has a high potential to act as an anticancer agent.



1. INTRODUCTION

Chemotherapy has been proved to be most effective in the treatment of cancer. Most of the drugs used for cancer treatment are platinum-based cytotoxic drugs. Although complexes based on heavy metals have great potential for cancer treatment, their use is limited by their undesirable side effects due to toxicity.^{1–6} Therefore, the growing demand for new anti-cancer drugs with reduced toxicity diverted the focus of chemotherapeutic research to non-platinum-based compounds that would serve as suitable alternatives.⁷ In this regard, copper compounds have attracted special attention on the assumption that copper being an endogenous metal, its complexes are expected to show lower toxicity than that of platinum compounds. Moreover, owing to their biologically accessible redox potential and having strong nucleobase affinity, copper complexes are of particular interest with respect to DNA damage.⁸ Not only the metal ion but also the nature of the ligand plays an important role in the efficacy of a metal complex to act as a potential drug because the ligand in

the metal complex plays vital role in its binding to DNA, which is considered to be the primary target for acting as an anticancer agent. Chelating ligands having N,S/O donors have biological relevance because several bioactive molecules possess a similar donor environment.⁹ Metal complexes with chelating ligands, which can effectively bind and are capable of cleaving DNA under physiological conditions, are considered to have potential to serve as anticancer agents. Several Cu(II) N,S,O/NN donor chelates are reported as potential anticancer agents owing to their ability for strong interaction with DNA base pairs.¹⁰ Most of the reported copper complexes exhibit oxidative DNA

Received: April 14, 2022

Accepted: June 1, 2022

Published: June 13, 2022



cleavage. Oxidative cleavage targets either the sugar moiety or the base of the DNA strands and is comparatively easier. DNA cleavage through an oxidative pathway requires a co-reagent such as an oxidizing or reducing agent and a light or metal center that is redox-active, apart from the principal cleaving agent. However, hydrolytic cleavage involves breaking of the phosphodiester bond that exists between individual nucleotides. The phosphodiester bond in DNA is extremely stable and therefore inert to cleavage under normal physiological conditions.^{11,12} Thus, to design compounds that are capable of cleaving DNA hydrolytically under physiological conditions without the aid of any chemical reagent or light is highly challenging.

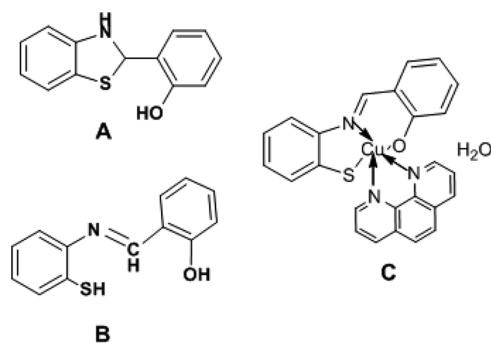
Another important aspect is the delivery of a drug to the target site, which determines the potential of a promising drug candidate. Hence, studies on binding of drugs to human serum albumin (HSA) like plasma proteins that serve as efficient drug carriers and are known to accumulate in tumors became vital in the development of anticancer agents.^{13–15}

In view of the above consideration, we have studied a copper(II) complex¹⁶ **1** containing an SNO-donor Schiff as the major ligand¹⁷ with an additional heterocyclic-N donor adduct to investigate its DNA binding and cleavage ability and anticancer and apoptosis induction activities. The binding interaction of **1** with the effective drug carrier HSA was also studied using different spectral and computational techniques. Thereafter, complex **1** was screened for its anticancer activity against HeLa human cervical and MDA-MB-231 breast cancer cells, and its apoptotic potential was investigated using nuclear staining techniques. Finally, in order to elucidate the apoptotic pathways activated by complex **1**, Western blotting analysis was performed to measure the expression of Bax, p53, and caspase 3, which are key regulators of the apoptotic pathway.

2. RESULTS AND DISCUSSION

2.1. Synthesis and Characterization. When $\text{Cu}(\text{OAc})_2 \cdot \text{H}_2\text{O}$ and 1,10-phenanthroline (1:1) in methanol were reacted with 2-(2-hydroxyphenyl)benzthiazoline (**A**, Scheme 1), it

Scheme 1. Proposed Structures for 2-(2-Hydroxyphenyl)benzthiazoline (A); In Situ Formation of a Schiff Base (B); and the Cu^{2+} Complex **1 (C)**



underwent rearrangement to produce the Schiff base in situ (**B**) followed by its coordination to the Cu^{2+} ion, forming the mixed ligand complex **1** containing the Schiff base that was found to coordinate to the Cu^{2+} ion as a SNO^- chelate¹⁷ and the co-ligand *o*-phen (**C**, Scheme 1) that was isolated as a solid along with a water molecule.

2.2. UHPLC-ESI-MS Spectra. Ultrahigh performance liquid chromatography–electrospray ionization mass spectrometry (positive ion mode) experiment of **1** in CH_3CN showed a peak at m/z 353.07 (Figure S1A, Supporting Information) corresponding to $[\text{Cu}_2(\text{C}_{13}\text{H}_8\text{NSO})]^+$, while the peak appeared at m/z 457.10 (Figure S1B, Supporting Information) due to a protonated oxidized Schiff base corresponding to $[(o\text{-HO-C}_6\text{H}_4\text{C}(\text{H})=\text{N-C}_6\text{H}_4\text{-S-o})_2 + \text{H}]^+$.

2.3. Infrared and Electronic Spectra. 2-(2-Hydroxyphenyl)benzthiazoline (**A**) displayed an IR peak at 3252 cm^{-1} (Figure S2A, Supporting Information) due to $\nu(\text{N-H})$ stretching, which disappears upon complex formation with Cu^{2+} (Figure S2B). This is consistent with the fact that 2-(2-hydroxyphenyl)benzthiazoline (**A**) undergoes rearrangement¹⁷ to form the Schiff base complex **1** in situ as confirmed from its X-ray crystal structure (Figure 1). The $\nu(\text{S-H})$ band near $2550\text{--}2600\text{ cm}^{-1}$ is not observed in the ligand or the complex. A strong peak at 1605 cm^{-1} which may be attributed to $\nu(\text{C}=\text{N})$, appeared in the IR spectrum of complex **1**. The acetonitrile solution of compound **1** exhibited strong charge-transfer electronic transitions in the $500\text{--}200\text{ nm}$ region (Figure S3, Supporting Information), while a d–d transition was observed as a weak and broad band centered around 800 nm .

2.4. EPR Spectra. The compound in its powder state displays strong X-band electron paramagnetic resonance (EPR) at both RT and liquid nitrogen temperature (LNT) (Figure S4), indicating its paramagnetic nature. The g values are found to be $g_{\parallel} = 2.1712$ and $g_{\perp} = 2.0739$ at RT and $g_{\parallel} = 2.1492$ and $g_{\perp} = 2.0641$ at LNT, respectively. On the other hand, a four-line pattern is displayed by the compound in acetonitrile at RT originating from the interaction of the unpaired electron with $^{63/65}\text{Cu}$ nucleus, $I = 3/2$, suggesting its monomeric nature in solution. The g_{iso} value is found to be 2.0939 , while A_{iso} is $\sim 8\text{ mT}$. LNT frozen glass EPR of **1** in CH_3CN exhibited a characteristic spectrum having a monomeric tetragonal character with $g_{\parallel} = 2.1479$ and $g_{\perp} = 2.0691$ and $A_{\parallel} \approx 18.0\text{ mT}$ and $A_{\perp} \leq 3.9\text{ mT}$, respectively.

2.5. X-ray Crystal Structure. The molecule crystallized in the monoclinic¹⁶ C centered crystal system with space group $C2/c$. The asymmetric unit of the crystal lattice contains one molecule of the copper complex and 0.625 molecule of water. The twofold axis of symmetry passes through the oxygen of the water molecules O2 and O3. It is to be noted that the water molecule O3 is disordered, and it is partially occupied at the twofold axis of symmetry. A free refinement of the O3 atom site showed that 0.125 oxygen only was present at the site. Hence, its occupancy is constrained at a value of 0.125 in the asymmetric unit of the crystal lattice. In such a scenario, hydrogen atom location is not possible from the single-crystal data. Hence, it is decided to ignore the hydrogens and leave the oxygen as it is. However, hydrogen atom counts are included in the formula given in the cif.

The central copper atom shows penta-coordination through the tri-dentate ligand and bi-dentate phenanthroline moiety. The metal complexes with penta coordination can have two possible co-ordination geometries, namely, square pyramid and trigonal bipyramid. In order to differentiate between these two geometries, a geometry index called tau (τ) has been proposed by Addison et al.,¹⁸ which is given as $\tau = (\beta - \alpha)/60$, where β and α are the largest basal angles. A τ value of 0 indicates a perfect square pyramid geometry, while for a perfect trigonal bipyramidal structure, it will be 1. The τ value of our copper complex is found to be $(177.23 - 164.63)/60 = 0.21$, which

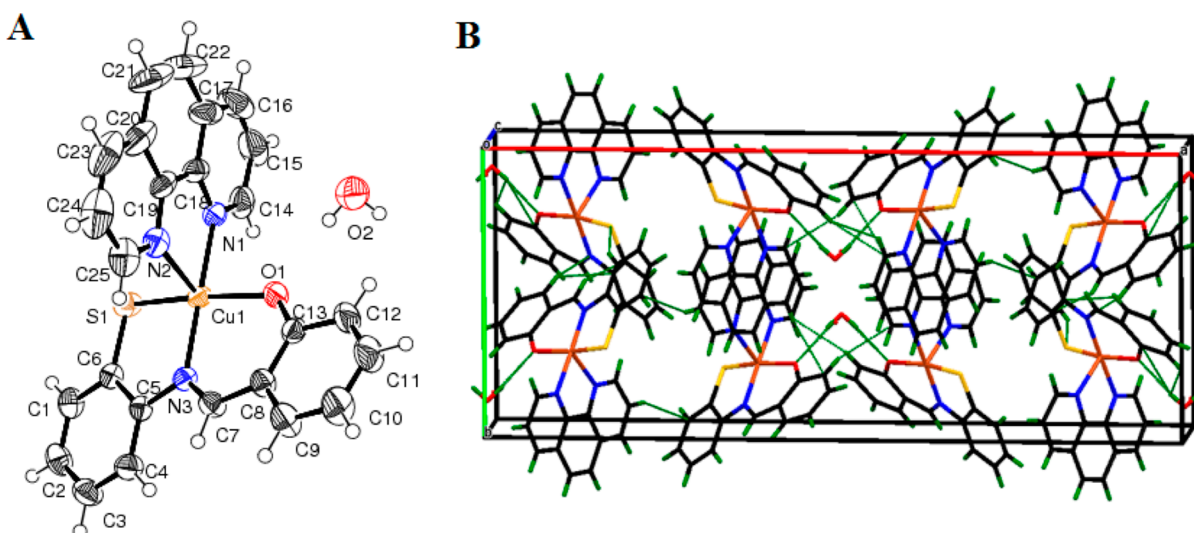


Figure 1. (A) ORTEP (50%) diagram of **1** (C14). (B) Packing of the molecule in the unit cell. Important bond lengths [Å] and angles [°] for **1**: Cu(1)–O(1) 1.9480(14), Cu(1)–N(3) 1.9738(17), Cu(1)–N(1) 2.0494(18), Cu(1)–S(1) 2.2605(6), Cu(1)–N(2) 2.2648(18); O(1)–Cu(1)–N(3) 93.48(6), O(1)–Cu(1)–N(1) 87.33(6), N(3)–Cu(1)–N(1) 177.23(7), O(1)–Cu(1)–S(1) 164.63(5), N(3)–Cu(1)–S(1) 87.76(5), N(1)–Cu(1)–S(1) 90.76(5), O(1)–Cu(1)–N(2) 93.28(7), N(3)–Cu(1)–N(2) 105.10(7), N(1)–Cu(1)–N(2) 77.49(7), S(1)–Cu(1)–N(2) 101.19(5).

indicates a distorted square pyramidal geometry for the copper complex. The base plane of the distorted square pyramid was formed by O1, N3, S1, N1, while the apex was formed by N2. The bond distances and angles of these atoms to the central copper are listed in Table S1.

In the crystal lattice, two molecules of copper complexes are held together by an O(2)–H(2A)···O(1) hydrogen bond interaction with a $d(\text{H}\cdots\text{A})$ distance of 2.11(2) Å [$\angle\text{DHA} = 174(3)$]. In addition to this, the crystal lattice is stabilized by CH···S, CH···N, and CH··· π interactions.

2.6. DNA Binding. 2.6.1. Spectrophotometric DNA Titration. Spectrophotometric DNA titration was performed to determine the binding mode and binding affinity of complex **1** with calf thymus DNA (CT-DNA). When a metal complex interacts with DNA, spectral transition of the complex is perturbed, and changes in the magnitude of absorbance and peak position occur. If a complex binds to DNA by intercalative mode, a decrease in the molar absorptivity (hypochromism) is observed, whereas hyperchromism may be expected for metal complexes that bind to DNA non-intercalatively or electrostatically.^{4,19} Absorption measurements were carried out by using a constant complex concentration (5×10^{-5} M) while increasing the concentration of CT-DNA until no change was visible on the UV–vis spectrum (Figure 2). As seen from the absorption titration study with complex **1**, hypochromicity of 79% was observed, clearly indicating intercalating binding that usually results from strong stacking of the aromatic chromophore in the DNA base pairs. The titration data were further used to calculate the intrinsic binding constant (K_b) from the slope to intercept ratio of the plot $[\text{DNA}]/(\epsilon_a - \epsilon_f)$ versus $[\text{DNA}]$ (Figure 2 inset). The calculated K_b value for complex **1** was found to be $7.88 \times 10^5 \text{ M}^{-1}$. Thus, from the spectrophotometric results, we may conclude that complex **1** has moderate binding affinity for DNA and possibly acts as an intercalator. This was further supported by the ethidium bromide (EB) displacement assay and finally confirmed from the enhanced viscosity of DNA that resulted with increasing amount of **1** as revealed from the viscosity measurement experiment described below.

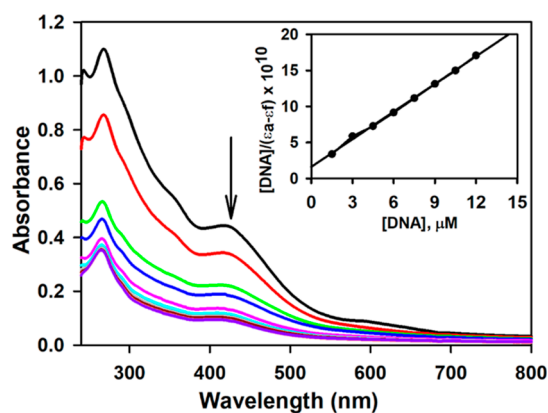


Figure 2. Effect on the electronic absorption spectra of complex **1** (5×10^{-5} M) with incremental addition of CT-DNA (0–12 μM) in 10 mM Tris–HCl having pH 7.4. Plot of $[\text{DNA}]/(\epsilon_a - \epsilon_f)$ vs $[\text{DNA}]$ shown in the inset.

2.6.2. Competitive DNA Binding: Fluorescence Studies. An EB displacement study was carried out to assess the relative binding affinity of complex **1** to CT-DNA with respect to EB, which is a conjugate planar molecule that emits weak fluorescence, but it is known to emit intense fluorescence at around 600 nm in the presence of DNA due to its complete intercalation between the adjacent base pairs of DNA. This enhanced fluorescence may be quenched by addition of a competing molecule as that will reduce DNA binding sites available for EB. When complex **1** was added to DNA pre-treated with EB, the fluorescence intensity decreased with increasing complex concentration (Figure 3A), suggesting that **1** was able to displace DNA-bound EB and binds to CT-DNA at the intercalation sites. The quenching data are in good agreement with the linear Stern–Volmer eq 1

$$\frac{F_0}{F} = 1 + K_{SV}[Q] \quad (1)$$

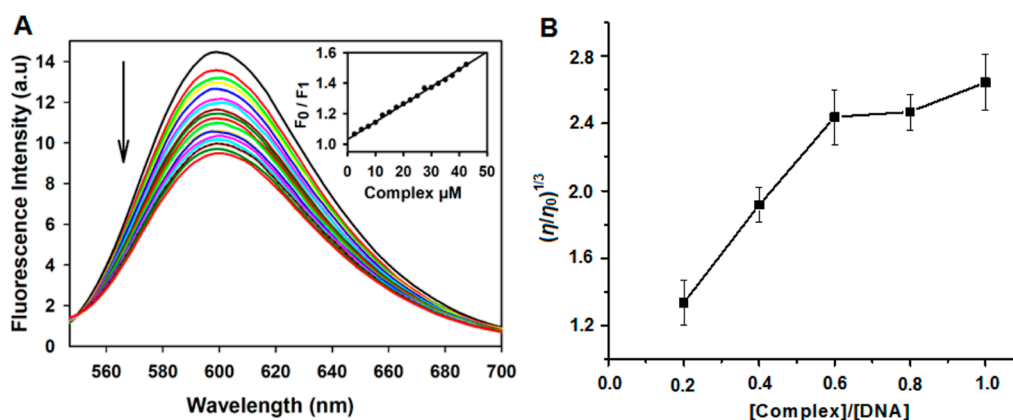


Figure 3. (A) Emission spectra of EB-bound CT-DNA in the absence (top black curve) and presence of complex **1**. $[\text{complex}] = 0$ to $42.5 \mu\text{M}$ at an increment of $2.5 \mu\text{M}$ in 10 mM Tris-HCl buffer ($\text{pH} = 8.0$). λ_{ex} was 510 nm . $[\text{EB}] = 2 \mu\text{M}$ and $[\text{CT-DNA}] = 50 \mu\text{M}$. The fluorescence intensity of EB-bound CT-DNA decreased with increasing amounts of **1**, as shown by the arrow. The inset shows the linear plot of F_0/F vs $[\text{complex}]$. (B) Effect of increasing concentration of **1** ($0, 20, 40, 60, 80,$ and $100 \mu\text{M}$) on the relative viscosity of CT-DNA ($100 \mu\text{M}$) in 10 mM Tris-HCl buffer ($\text{pH} 7.4$) at RT.

where F_0 and F represent the fluorescence intensities in the absence and presence of a quencher (complex **1**), respectively. K_{SV} is the linear Stern–Volmer quenching constant and $[\text{Q}]$ denotes the complex concentration. The K_{SV} value was determined from the ratio of the slope to intercept of the F_0/F versus $[\text{Q}]$ (Figure 3A, inset) plot and was found to be $1.12 \times 10^4 \text{ M}^{-1}$ ($R^2 = 0.99$ for 18 points), suggesting strong affinity of complex **1** to CT-DNA.

Further, the apparent binding constant was determined using eq 2.

$$K_{\text{EB}} \times [\text{EB}] = K_{\text{app}} \times [\text{complex}]_{50} \quad (2)$$

where $[\text{complex}]_{50}$ denotes the concentration of the complex at which the intensity of fluorescence is reduced to 50% of the initial EB-DNA adduct. $K_{\text{EB}} = 1 \times 10^7 \text{ M}^{-1}$, $[\text{EB}] = 2 \times 10^{-6} \text{ M}$. The apparent binding constant was found to be $1.32 \times 10^6 \text{ M}^{-1}$, which appears to be 10-fold lower than the binding constant of the classical intercalator.

2.7. Viscosity Measurement. To support the intercalative mode of DNA binding as suggested from spectroscopic analysis, a viscosity measurement experiment was performed to find out the effect of increasing concentrations of **1** on CT-DNA. It is known that an intercalative mode of DNA binding leads to a significant increase in viscosity because insertion of an intercalator causes the base pairs of DNA to separate and unwind, resulting in an increase in the overall length of the DNA, thereby increasing the viscosity. Based on our experimental results, the plot for the relative viscosity $(\eta/\eta_0)^{1/3}$ versus $[\text{complex}]/[\text{DNA}]$ (Figure 3B) clearly showed that there is a steady increase in viscosity, confirming the intercalative mode of binding of complex **1** to CT-DNA.

2.8. DNA Cleavage. pUC19 DNA cleavage promoted by **1** was investigated by agarose gel electrophoresis. The pUC19 plasmid DNA has a compact supercoiled (SC) conformation (form I), and when subjected to electrophoresis, it migrates relatively fast. Single-strand scission of this SC form of DNA generates a slower moving nicked circular (NC) form (form II), and on double-strand scission, a linear form (form III) that migrates between SC and NC forms is generated.^{20,21} Generally, DNA cleavage^{22–24} can occur by three ways, namely, (i) DNA hydrolysis, (ii) oxidative cleavage, and (iii) photochemical cleavage, of which the last two categories are closely related. In

the oxidative cleavage pathway, the target is either a sugar moiety or the base of the DNA strands and is comparatively easier. The oxidative process leads to generation of reactive species such as the hydroxyl radical ($\cdot\text{OH}$) or singlet oxygen ($^1\text{O}_2$), involving either a photolytic or a redox active metal center causing DNA damage. On the other hand, hydrolytic cleavage involves breaking of the phosphodiester bond, which exists between individual nucleotides, that is, the building blocks of DNA. The phosphodiester bond is extremely stable, having an estimated half-life of hundred billions of years and is therefore inert to cleavage under normal physiological conditions.^{25,26} This means that, for effective hydrolysis of the phosphate backbone, a catalyst has to accelerate the hydrolysis rate to such an enormous extent that it is achievable within a perceivable time frame (say, couple of minutes or hours), which is highly challenging. Thus, reagents that can hydrolytically cleave DNA without the aid of any external agent or light hold extreme importance. Most of the reported Cu(II) compounds are able to cleave DNA following an oxidative pathway in the presence of a co-reagent such as ascorbate or peroxide, but only a few of them are able to bring about DNA cleavage hydrolytically without any co-reagent.^{26–28}

We have performed DNA-cleavage studies using both oxidative and hydrolytic conditions. It was observed that complex **1** in the presence of H_2O_2 cleaved pUC19 DNA oxidatively, and successive conversion of the SC form to the nicked form was observed in a concentration-dependent manner (Figure 4A). At a $0.5 \mu\text{M}$ concentration of **1**, there was 36% conversion to the nicked form (Figure 4A, lane 2), and a 100% conversion was observed at as low a concentration as $2 \mu\text{M}$ of complex **1** (Figure 4A, lane 4). Thus, complex **1** proves to be highly efficient in conducting oxidative single-strand scission of DNA. In order to verify the role of free radicals such as the hydroxyl radical and singlet oxygen in oxidative cleavage, scavengers such as DMSO ($2 \mu\text{L}$) for $\cdot\text{OH}$ and NaN_3 ($500 \mu\text{M}$) for $^1\text{O}_2$ were used (Figure 4B, Lane 3 and Lane 4, respectively). It was observed that there was significant inhibition in DNA cleavage in the presence of DMSO, but no such considerable inhibition was observed in the case of NaN_3 . Therefore, it can be inferred that hydroxyl radicals are majorly driving the oxidative DNA cleavage.

Further, to explore if complex **1** was capable of cleaving DNA hydrolytically, the cleavage activity was studied in the absence of

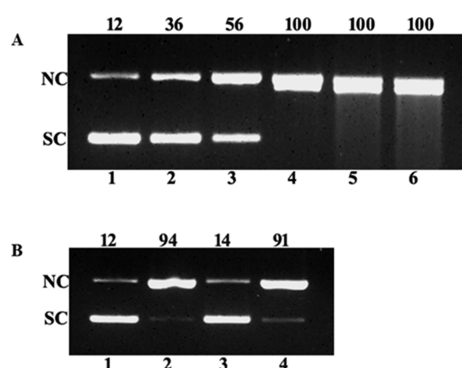


Figure 4. Oxidative cleavage of pUC19 DNA (200 ng) in 50 mM Tris–HCl buffer (pH 8) at 37 °C. (A) Lane 1, pUC19 DNA + H₂O₂ (1 mM) control; lane 2, pUC19 DNA + **1** (0.5 μM) + H₂O₂ (1 mM); lane 3, pUC19 DNA + **1** (1 μM) + H₂O₂ (1 mM); lane 4, pUC19 DNA + **1** (2 μM) + H₂O₂ (1 mM); lane 5, pUC19 DNA + **1** (3 μM) + H₂O₂ (1 mM); lane 6, pUC19 DNA + **1** (4 μM) + H₂O₂ (1 mM). (B) Cleavage in the presence of ROS scavengers: Lane 1, pUC19 DNA + H₂O₂ (1 mM) control; lane 2, pUC19 DNA + **1** (2 μM) + H₂O₂ (1 mM); lane 3, pUC19 DNA + **1** (2 μM) + H₂O₂ (1 mM) + DMSO (2 μL); lane 4, pUC19 DNA + **1** (2 μM) + H₂O₂ (1 mM) + NaN₃ (500 μM).

any external reagent or light. Complex **1** was found to mediate rapid conversion of pUC19 DNA from the SC form (form I) into the nicked form (form II). As seen in Figure 5 (lane 5), at a

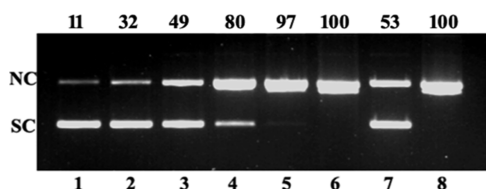


Figure 5. Hydrolytic cleavage of pUC19 DNA (200 ng) at 37 °C in 50 mM Tris–HCl buffer, pH 8. Lane 1, only pUC19 DNA as control; lane 2, pUC19 DNA + **1** (5 μM); lane 3, pUC19 DNA + **1** (10 μM); lane 4, pUC19 DNA + **1** (25 μM); lane 5, pUC19 DNA + **1** (50 μM); lane 6, pUC19 DNA + **1** (100 μM); lane 7, pUC19 DNA + **1** (100 μM) + DMSO (2 μL); lane 8, pUC19 DNA + **1** (100 μM) + NaN₃ (500 μM).

concentration of 50 μM, there was 97% conversion into the nicked form under hydrolytic conditions, which is quite remarkable. To see if any oxidant is present in the reaction mixture that leads to ROS formation, control experiments were also performed in the presence of ROS scavengers such as DMSO and NaN₃ (lanes 7–8). It was observed that in the presence of DMSO ($\cdot\text{OH}$ scavenger), the conversion of the SC to the NC form was inhibited partially, while no such inhibition was seen in the presence of NaN₃ ($^1\text{O}_2$ scavenger), suggesting that some amount of oxidants are present in the reaction mixture and produce $\cdot\text{OH}$ radicals that also contribute to the DNA cleavage. Therefore, we may infer that the observed DNA cleavage was not purely hydrolytic. Therefore, it may be concluded that complex **1** is moderately capable of hydrolytic DNA cleavage while it is quite efficient in carrying out oxidative cleavage, and this is a very important attribute for any anti-tumor metal complex.²⁹

To determine the hydrolytic cleavage rate, the kinetics of hydrolytic DNA cleavage was studied. The cleavage reaction was monitored using agarose gel electrophoresis to assess the effect of **1** (200 μM) on pUC19 DNA (200 ng) using 50 mM Tris–HCl buffer at 37 °C with time. As seen in Figure 6A, when

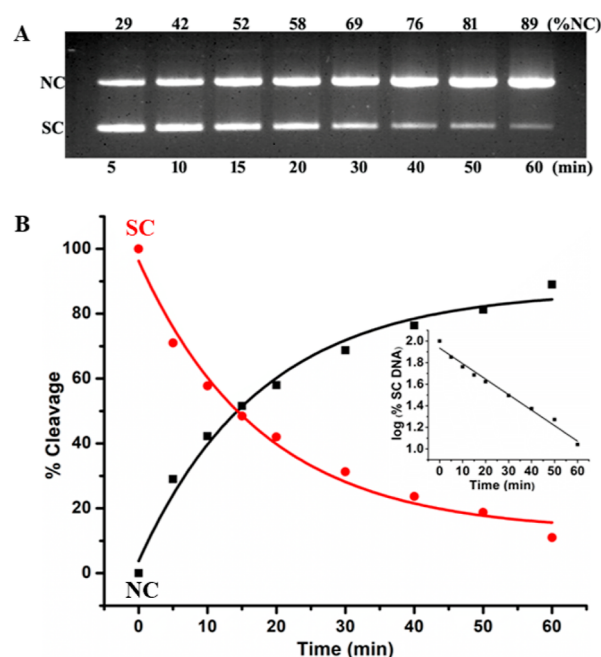


Figure 6. Time course measurement: (A) gel image showing the position of the SC and NC forms as marked on the left of the gel and % conversion to the NC (on top) form with time. (B) Cleavage activity showing the disappearance of SC DNA and formation of NC DNA with increasing incubation time in the dark at 37 °C; the inset shows the plot of log(% SC DNA) vs time.

treated with complex **1**, pUC19 DNA gradually converted from SC DNA (form I) to NC DNA (form II) with time. A time-dependent decrease of form I fits well into a single exponential decay curve (Figure 6B), and the plot of log(% SC) against time showed a linear fit (Figure 6B, inset). The hydrolytic rate constant (k_{obs}) was determined from its slope and was found to be 1.987 h⁻¹. Thus, **1** increased the cleavage rate enormously (5.52×10^7 times) as compared to the uncatalyzed hydrolysis rate reported for ds-DNA ($k = 3.6 \times 10^{-8}$ h⁻¹). This enhanced rate of DNA hydrolysis by complex **1** is comparable with most of the reported synthetic hydrolases that are based on transition metals.^{25,28,30–33}

2.9. HSA Binding Ability. Drugs are usually transported to the target site on binding to plasma proteins; thus, the binding of a drug to plasma protein is important. HSA is the most abundant protein in human blood plasma. The absorption, distribution, transportation, and metabolism of a drug depend to a great extent on the binding ability of the drug to HSA.

2.9.1. Fluorescence Quenching. We have conducted binding studies of **1** with HSA using fluorescence spectroscopy. The intrinsic fluorescence of HSA arises mainly from the three amino acid residues, namely, tryptophan, tyrosine, and phenyl alanine; however, the emission fluorescence of HSA may be confined to that of tryptophan by exciting at 295 nm. The fluorescence spectra were recorded before and after titrating with **1**, and the fluorescence intensity of HSA at ~345 nm was observed to gradually decrease with increasing concentration of **1** (Figure 7). Addition of **1** to the HSA solution resulted in a significant decrease of 72.5% of the initial fluorescence intensity of HSA, which suggests a definite interaction of the compound with HSA. The observed quenching of fluorescence can be described by the Stern–Volmer relation (3)

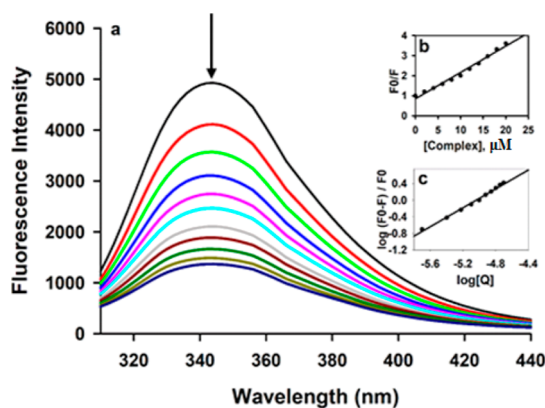


Figure 7. Emission spectra of 4 μM HSA ($\lambda_{\text{ex}} = 295 \text{ nm}$) in the presence of increasing amounts of complex **1**. (a) Black curve shows the fluorescence intensity in the absence of **1**. Fluorescence intensity quenched upon addition of increasing amounts of the compound as shown by the arrow. (b) Stern–Volmer plot and (c) modified Stern–Volmer plot of the complex with HSA are shown in the inset.

$$\frac{F_0}{F} = 1 + K_{\text{SV}}[Q] = 1 + k_q\tau_0[Q] \quad (3)$$

where F_0 is the fluorescence of HSA alone, F is the fluorescence after adding compound **1**, $[Q]$ is the molar concentration of **1** (quencher), and K_{SV} is the Stern–Volmer quenching constant. k_q is the bimolecular quenching rate constant and τ_0 is the average lifetime of the fluorophore in the absence of a quencher (τ_0 of HSA = 5.71 ns).

The slope of the Stern–Volmer eq 3 resulted in a high K_{SV} value ($1.31 \times 10^5 \text{ M}^{-1}$), indicating the strong quenching ability of **1**. The two mechanisms by which quenching can take place are static and dynamic quenching. As the calculated rate constant of the quenching process k_q is $2.29 \times 10^{13} \text{ M}^{-1} \text{ s}^{-1}$ (from eq 3), which is found to be 1000-fold higher than the value of the maximum scattering collision quenching constant ($2.0 \times 10^{10} \text{ M}^{-1} \text{ s}^{-1}$), it implies that the quenching of HSA fluorescence by **1** takes place by the static quenching process. The fluorescence quenching data were further used to evaluate the binding constant (K_a) and the binding site number (n) from the double logarithmic plot obtained following the relation 4

$$\log \frac{(F_0 - F)}{F} = \log K_a + n \log [Q] \quad (4)$$

where K_a is the binding constant and n is the number of binding sites per HSA.

The value of n (1.13) obtained from the slope of eq 4 being very close to 1 strongly supports the presence of one binding site for **1** in the neighborhood of the tryptophan residue of HSA, while the high binding constant K_a ($5.22 \times 10^5 \text{ M}^{-1}$) evaluated from the intercept suggests a strong binding affinity of complex **1** toward HSA.

2.9.2. UV–Vis Spectral Measurement. Electronic spectral measurement is another method that has been used to support the observed static quenching involved in the fluorescence measurement experiments discussed above. Dynamic quenching only affects the excited states of the fluorophores, and changes in absorption spectra are not expected, while unlike dynamic quenching, static quenching arising from ground-state HSA–complex formation is associated with changes in the electronic absorption spectra of HSA. Therefore, we have conducted electronic spectral studies of HSA with and without adding **1**.

Figure 8 shows a drastic decrease in absorbance at 219 nm along with a large red shift of 13 nm. The decrease in absorbance

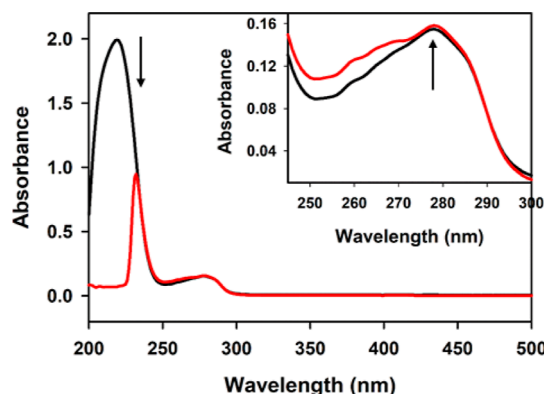


Figure 8. HSA (4 μM) absorption spectra: black curve, without and red curve, with 4 μM of complex **1**. The change in intensity around the 280 nm peak is shown in the inset.

supports the static quenching mechanism, and the associated large red shift of 13 nm clearly indicates the alteration in the protein secondary structure. Apart from this, a slight increase in absorbance is seen at 280 nm (Figure 8 inset), which indicates minor conformational changes in tertiary structures around amino acid residues.

The above results strongly suggest that the quenching of HSA fluorescence by **1** was due to static quenching owing to its complex formation in the ground state.

2.9.3. Synchronous Fluorescence Analysis. The synchronous fluorescence spectra were obtained by simultaneously scanning both the excitation and emission wavelengths, keeping a constant wavelength difference ($\Delta\lambda$) between them. The intrinsic fluorescence of HSA is mainly due to the emission of tryptophan and tyrosine residues.^{14,34–36} When $\Delta\lambda = 15 \text{ nm}$, the fluorescence intensity was quenched by 63.3% from 3314 to 1206 au (Figure 9A) without any change in wavelength maxima ($\lambda_{\text{max}} = 298 \text{ nm}$) and when $\Delta\lambda = 60 \text{ nm}$, the fluorescence intensity was quenched by 64.2% from 7414 to 2652 au (Figure 9B), again without any change in the wavelength maxima ($\lambda_{\text{max}} = 340 \text{ nm}$). The significant decrease in fluorescence intensity observed in both cases ($\Delta\lambda = 15$ and 60 nm) suggests that complex **1** possibly binds to HSA in the vicinity of tyrosine and tryptophan residues.

2.9.4. 3D Fluorescence Studies. It is a powerful tool used to get conformational and structural information of proteins. The 3D fluorescence spectra for HSA (4 μM) and HSA–complex **1** (molar ratio 1:1, each 4 μM) and corresponding data obtained therein are shown in Figure 10 and Table 1. Peak 1 obtained when $\lambda_{\text{ex}} = 280 \text{ nm}$ reflects the spectral characteristics of tryptophan (Trp) and tyrosine (Tyr) amino acid residues of HSA. Peak 2 obtained when $\lambda_{\text{ex}} = 230 \text{ nm}$ is the feature of protein 3D fluorescence that is due to emission corresponding to the protein backbone.^{37–39} As seen in Figure 10 and Table 1, the fluorescence intensity of peak 1 has decreased significantly by 32% with the addition of complex **1**, and the possible reason might be the binding of **1** to HSA near the Trp and Tyr residues, thus inducing some conformational and micro-environmental changes around these amino acids. Also, a marked 61% decrease in the intensity of peak 2 was observed and it was accompanied with a blue shift of 4 nm, suggesting alteration in the polypeptide backbone structure. From these observations, we may suggest

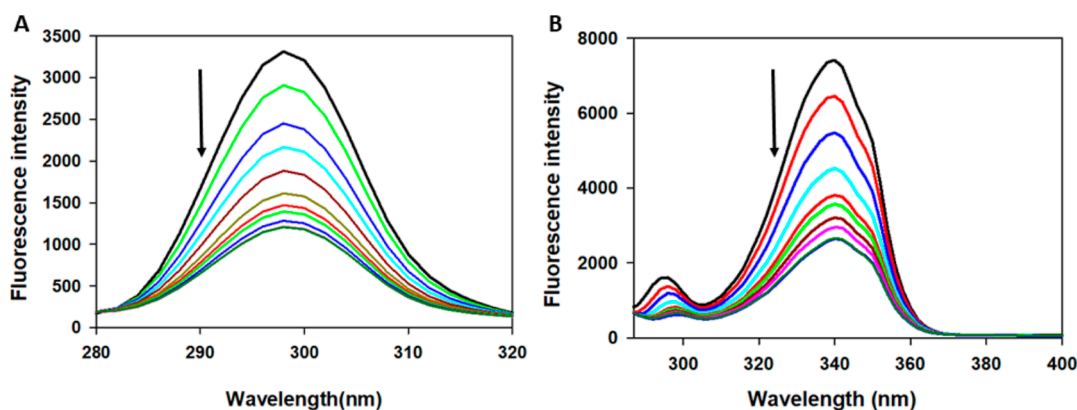


Figure 9. Synchronous fluorescence spectra of 4 μM HSA in 20 mM sodium phosphate buffer at pH 7.4 upon addition of (A) complex 1 (0–12 μM), $\Delta\lambda = 15$ nm; (B) complex 1 (0–12 μM), $\Delta\lambda = 60$ nm.

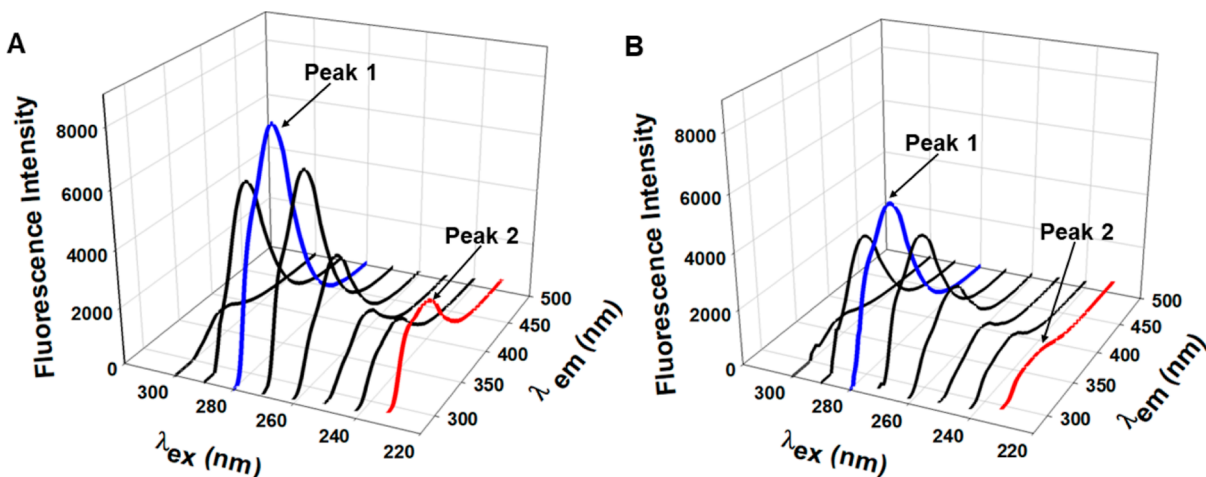


Figure 10. HSA 3D fluorescence spectra recorded without and with 1: (A) HSA only (4 μM), (B) HSA (4 μM)/1 (4 μM).

Table 1. 3D Fluorescence Results

	peak 1			peak 2		
	peak position ($\lambda_{\text{ex}}/\lambda_{\text{em}}$)	fluorescence intensity (AU)	$\Delta\lambda$ (nm)	peak position ($\lambda_{\text{ex}}/\lambda_{\text{em}}$)	fluorescence intensity (AU)	$\Delta\lambda$ (nm)
HSA	280/338	7766	58	230/334	2891	104
HSA + 1 (1:1)	280/338	5288	58	230/330	1136	100

that complex 1 on binding to HSA has altered the tertiary and secondary structures of the protein.

2.10. Energy Transfer from HSA to Complex 1. The quenching of fluorescence of HSA upon binding to complex 1 indicates that there is energy transfer between HSA and complex 1, which can be explained by the fluorescence resonance energy transfer (FRET) theory. According to this theory, three conditions have to be satisfied for the energy transfer to take place: (1) the donor should be fluorescent, (2) there should be sufficient overlap between the fluorescence emission spectrum of the donor and UV–vis absorbance spectrum of the acceptor, and (3) the distance between the donor and acceptor should be within 8 nm. The efficiency of energy transfer, E , from HSA (Trp214) to complex 1 can be determined using eq 5

$$E = \frac{R_0^6}{R_0^6 + r^6} = 1 - \frac{F}{F_0} \quad (5)$$

where E denotes the efficiency of energy transfer, R_0 is the critical distance at which the efficiency of energy transfer is 50%,

and r is the average distance between the donor and acceptor. F and F_0 are the fluorescence intensities of the donor (HSA) with and without the acceptor (complex 1). Also, R_0 can be calculated^{35,40} using eq 6

$$R_0 = 0.02108(K^2\phi N^{-4}J)^{1/6} \quad (6)$$

where K^2 is the spatial orientation factor, N denotes the refractive index of the medium, ϕ is the fluorescence quantum yield of the donor, and J is the overlap integral of the donor emission spectrum and the acceptor absorption spectrum. In this study, K^2 , ϕ , and N for HSA are considered as 2/3, 0.118, 1.33, respectively.³⁹

Again the J value can be determined⁴⁰ from eq 7

$$J = \int I_D(\lambda)\epsilon_A(\lambda)\lambda^4 d\lambda \quad (7)$$

where $I_D(\lambda)$ denotes the normalized fluorescence intensity of the donor of wavelength λ and $\epsilon_A(\lambda)$ is the extinction coefficient of the acceptor at λ .

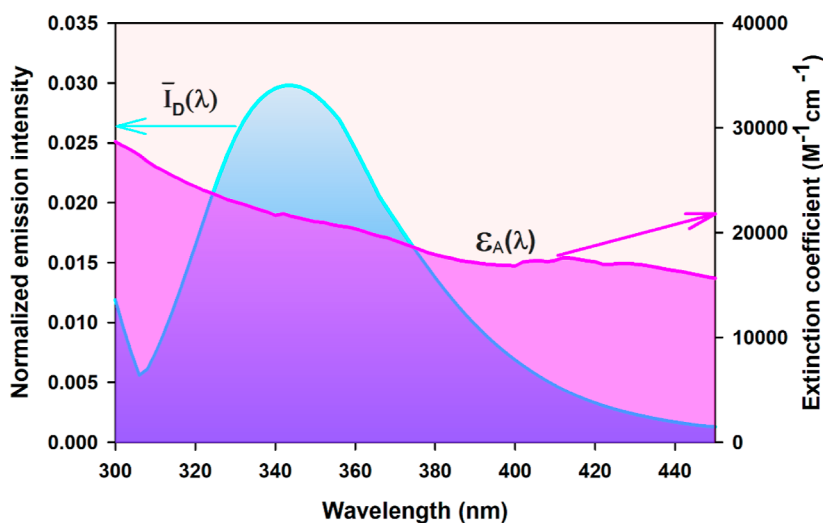


Figure 11. Spectral overlap between HSA ($4 \mu\text{M}$) and **1** ($4 \mu\text{M}$): the normalized emission spectrum of the donor HSA (blue, left), molar extinction coefficient spectrum (pink, right) of acceptor complex **1**, and the resulting spectral overlap (violet).

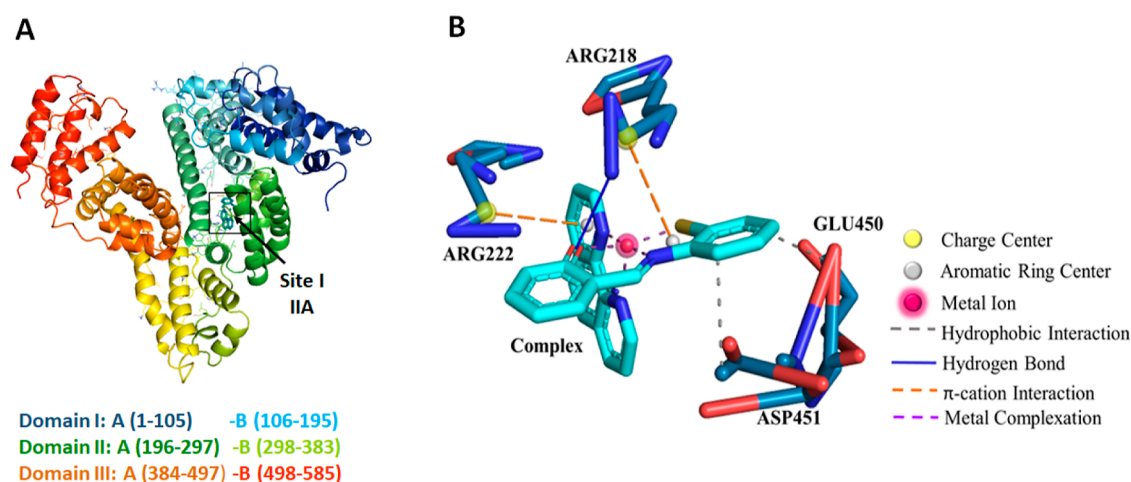


Figure 12. Molecular docking of HSA with complex **1**. (A) Full view of HSA with color-coded subdomains showing the binding site of **1** in HSA. (B) Detailed interactions of **1** with surrounding amino acid residues.

The overlap between the fluorescence spectrum of HSA and the absorbance spectrum of complex **1** is shown in Figure 11. By using the above equations, the values of E , J , R_0 , and r for the HSA–complex **1** system were found to be 0.27, $3.308 \times 10^{14} \text{ nm}^4 \text{ M}^{-1} \text{ cm}^{-1}$, 3.003 nm, and 3.52 nm respectively. From these results, we see that the calculated value of r is within the range $2 < r < 8$ nm, and the value of r is such that r is $> 0.5R_0$ and $< 1.5R_0$. Thus, the conditions for FRET to occur were met, and there is a high possibility of energy transfer from HSA to complex **1**.

2.11. Molecular Docking Analysis. HSA, being the most abundant circulating protein present in blood plasma, plays a crucial role in binding and transporting exogenous compounds such as pharmacological drugs; therefore, it is important to assess the types and extent of their binding interactions with HSA. As seen in Figure 12A, HSA is a helical heart-shaped protein consisting of 585 amino acid residues grouped in three domains (I, II, and III), each of which is further subdivided into six-helix and four-helix subdomains termed A and B. In HSA, there are two high-affinity binding sites for drugs, namely, Sudlow's site 1 (in subdomain IIA) and Sudlow's site 2 (in subdomain IIIA).⁴¹ Molecular docking computations were done to gain information about the binding conformations of complex

1 with the active site of HSA. Out of 20 docking conformations obtained, the best docking pose was selected for analysis, and the binding energy was found to be -8.4 kcal/mol. The specific binding interaction of complex **1** with the surrounding amino acid residues present in the binding site and its vicinity is displayed in Figure 12B with labeled key residues. Further, a protein–ligand interaction profiler⁴² was used for visualization and comprehensive analysis of the interactions detected between the target protein molecule (HSA) and ligand, and details of these interactions listed at the atom level is presented in Table 2. A strong hydrogen bond interaction (2.42 \AA) was observed between 1HH2 of Arg218 and O1 (phenolate O^-) of the Schiff base ligand coordinated to Cu1. Two hydrophobic interactions were observed, one of which is between the C1 atom of complex **1** and Glu450 and the other between the C4 atom of complex **1** and Asp451. However, these interactions are comparatively milder as indicated by their distance (Table 2). Also, two π –cation interactions were seen that involve binding between an aromatic π system and a nitrogenous cation. One of them arises from the centroid of the aromatic ring formed from S1, N3, C5, C6, and Cu1 of complex **1** [Figures 12B and 1A, Oak Ridge thermal ellipsoid plot (ORTEP) diagram] to the

Table 2. Metal Complexation and Detailed Molecular Interactions of Complex 1 with HSA

	index	residue	distance (Å)	complex atom ^a	residue atom ^{a,b}		
hydrogen bond interaction	1	ARG218	2.42	O1	1HH2		
hydrophobic interaction	1	GLU450	3.78	C1	CD		
	2	ASP451	3.77	C4	CG		
	index	residue	residue atoms ^{a,b} (charge center)	distance (Å)	offset (Å)	protein charged	complex atoms ^a (aromatic ring center)
π -cation interaction	1	ARG218	NE, NH1, NH2	3.87	0.92	✓	S1, N3, C5, C6, Cu1
	2	ARG222	NE, NH1, NH2	4.11	0.85	✓	N1, C14, C15, C16, C17, C18
	index	metal atom	ligand atom ^a	distance (Å)	angle (degree)	estimated geometry	
metal complexation	1	Cu	N1	2.05	N1–Cu1–O1 (87.32)	square pyramidal	
	2	Cu	O1	1.95	N3–Cu1–O1 (93.51)		
	3	Cu	S1	2.26	N2–Cu1–S1 (101.18)		
	4	Cu	N2	2.27	N1–Cu1–N2 (77.52)		
	5	Cu	N3	1.97	S1–Cu1–N3 (87.77)		

^aThe first one or two characters of the atom name comprise chemical symbols used to denote the atom type. The atom names that begin with “C” are carbon atoms; those beginning with “N” are nitrogen; those beginning with “S” are sulfur; and those beginning with “O” indicate oxygen atoms.

^bIn amino acid residues, the next character denotes the remoteness indicator code, which is represented as “D” for δ ; “E” for ϵ ; “G” for γ ; and “H” for η . (The structure of complex 1 with labeled atoms shown in Figure 1A was used in molecular docking.) The default threshold parameters used by PLIP to detect interactions are cut-off distance between the donor and the acceptor in hydrogen bond was 4.1 Å and the distance cutoff for identifying hydrophobic interactions between carbon atoms was 4 Å and for π -cation interaction two thresholds were applied, a 6 Å cut-off from the charge center to the centroid of the aromatic ring and the offset between the charge and the ring center within 2 Å.

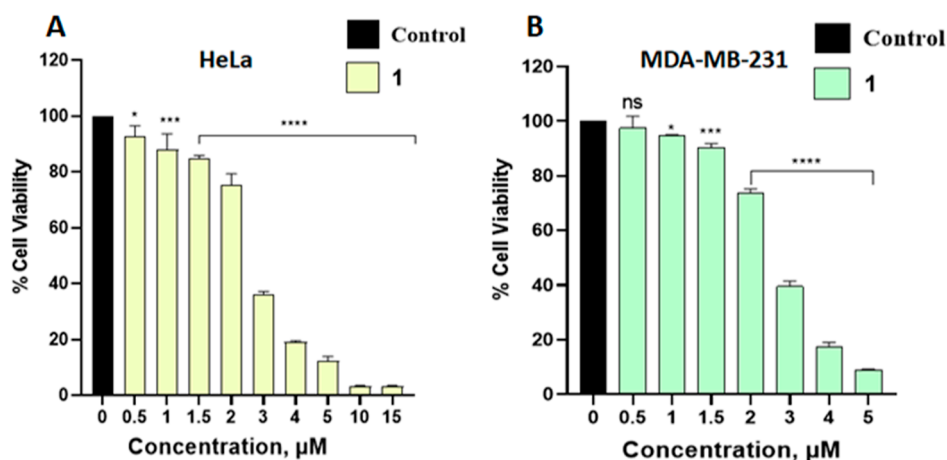


Figure 13. Percentage of cell viability for (A) HeLa and (B) MDA-MB-231 cells exposed to different concentrations of complex 1 followed by 24 h of incubation. Statistical analysis was done with the help of graph pad prism. **** indicates $p < 0.0001$. *** indicates $p < 0.001$. * indicates $p < 0.1$ and is not significant.

nitrogenous charge center of the Arg218 residue and the other arises from the centroid of the aromatic ring of *o*-phenanthroline (co-ligand) comprising N1, C14, C15, C16, C17, and C18 atoms to the nitrogenous charge center of Arg222 (Figures 12B and 1A, ORTEP diagram). Therefore, the collective information gathered from docking analysis shows that 1 mainly binds in subdomain IIA of HSA and most importantly, it interacts with residues such as Arg218 and Arg222 that are situated at the opening of Sudlow's site 1 in subdomain IIA, where the tryptophan residue (Trp214), which is the dominant intrinsic fluorophore of HSA, is also located. From these findings, we may conclude that complex 1 binds near Trp214, and it would be relevant to suggest that the energy transferred from the excited Trp214 to complex 1 results in subsequent quenching of HSA fluorescence; thus, the docking results are in good agreement with the experimentally observed spectroscopic results.

2.12. Cell Viability. The 3-(4,5-dimethylthiazol-2-yl)-2,5-diphenyltetrazolium bromide (MTT) assay was used to evaluate the inhibitory effects of complex 1 on the growth of HeLa

(cervical) and MDA-MB-231 (breast) cancer cells. The cells were incubated with varying amounts of 1 at 37 °C for 24 h, and control cells (untreated) were also maintained under the same experimental conditions for comparison. The results demonstrated that complex 1 significantly reduced the viability in a dose-dependent manner in the case of both cancer cell lines (Figure 13). For HeLa, at as low a concentration as 3 μM , the cell viability was reduced to a mere 36% and for MDA-MB-231, it was 37%. As reflected from their IC_{50} values, complex 1 appeared to be almost equally toxic toward both HeLa ($2.63 \pm 0.11 \mu\text{M}$) and MDA-MB-231 ($2.68 \pm 0.09 \mu\text{M}$) cells. It is to be noted here that the free ligands with a 5 μM concentration, for example, have negligible cytotoxic effects on both these cell lines (Figure S5) when compared to that of 1 at the same 5 μM concentration, suggesting that the cytotoxic effect shown in Figure 13 originates from the intact complex and not from the ligand components.

2.13. Nuclear Hoechst Staining. Cell staining is a valuable technique for the assessment of apoptosis, enabling identi-

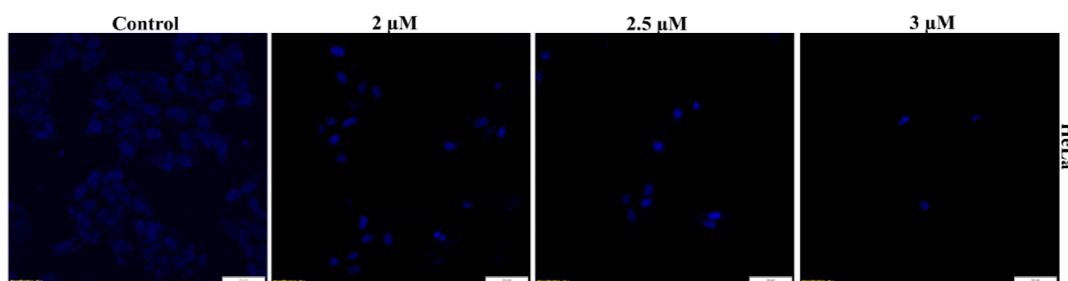


Figure 14. Fluorescence microscopic images of Hoechst-33342 stained HeLa cells post 24 h treatment with complex 1.

fication of the classical hallmarks of apoptosis such as membrane blebbing, cell shrinkage, chromatin condensation, and formation of apoptotic bodies.^{43,44} The control and complex 1-treated HeLa cells were stained with Hoechst 33342 and viewed under a confocal microscope (Figure 14). The control cells permeabilized with 0.1% Triton X-100 appeared light, having evenly stained contours of the nuclei, while the treated cells provide evidence of morphological changes such as blebbing, cell shrinkage, and apoptotic body formation attributed to the typical features of apoptotic cells (Figure S6). Thus, the Hoechst staining suggests apoptotic cell death promoted by 1.

2.14. Morphological Changes with AO and PI Dual Staining. Apoptotic cells show increased plasma membrane permeability to certain fluorescent dyes. Acridine orange (AO) is a cell membrane permeable dye that is taken up by viable and early apoptotic cells and emits green fluorescence. However, propidium iodide (PI) is an intercalating dye that binds to the DNA of late apoptotic and secondary necrotic cells emitting orange fluorescence.^{45,46} An AO/PI dual staining experiment was used to differentiate between live cells and dead cells based on their morphological changes assessed by fluorescent microscopic analysis. HeLa cells were incubated with 1 for 24 h, stained simultaneously with AO and PI, and viewed under a fluorescence microscope. As seen in Figure 15, the control comprising live cells show intact shape and were stained with AO emitting green fluorescence. The cells treated with 2 and 2.5 μM of 1 have undergone distinct morphological alteration, showing significant orange to green fluorescence, characteristic of early apoptotic cells. At a 3 μM concentration, comparatively few cells were visible; the cells appear to be rounded and shrunken, bearing reddish orange nuclei, indicating that the cells may have reached the late stage of apoptosis.

2.15. Morphological Alterations Viewed Using Phalloidin Staining. In order to visualize the effect of complex 1 on cytoskeletal actin filaments, HeLa cells were stained using phalloidin-iFluor 488 along with Hoechst 33342. Actin plays an important role in many biological functions such as cytokinesis, endocytosis, cell motility, intracellular organization, vesicle trafficking, and also apoptosis.⁴⁷ Studies have shown that fragmentation of actin filaments could lead to shrinking of cells as well as downstream caspase activation, which would lead to apoptosis. All this makes actin a suitable target for anti-cancer drugs. In our experiment, we found that (Figure 16) the control cells display intact actin filaments (green) as well as intact nuclei (blue), and treated cells clearly show loss of actin filaments and nuclear fragmentation. At a 2 μM dose itself, the damage to actin filaments is clearly visible (Figure 16); further with increasing concentration of 1, the morphology of HeLa cells changed, which may indicate stress, along with clear nuclear fragmentation and destruction of actin filaments, which might lead to

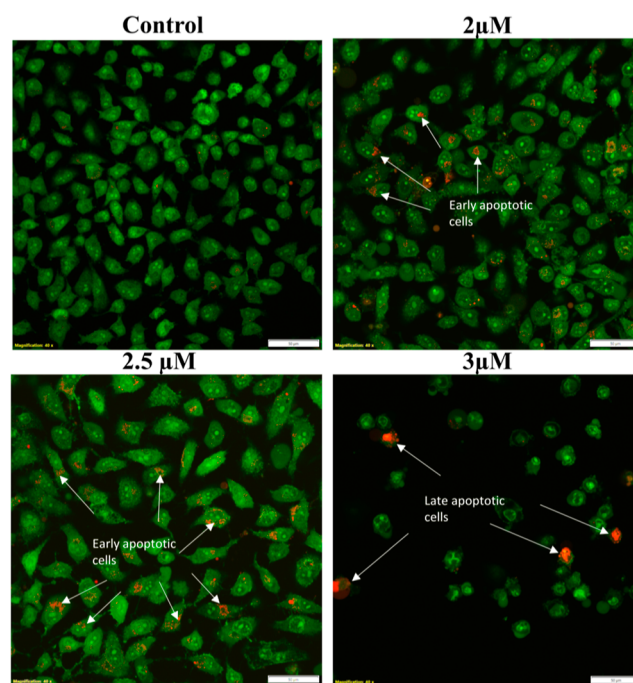


Figure 15. Confocal microscopy images of HeLa cells treated with different doses of complex 1 followed by AO/PI dual staining post 24 h of treatment. The arrows indicate early apoptotic cells bearing orange to green fluorescence and late apoptotic cells bearing reddish orange nucleus.

reduction in motility, cytokinesis, and even apoptosis^{48,49} and could be an important anticancer attribute.

2.16. Western Blot Analysis. To investigate the role of complex 1 in inducing apoptosis in cancer cells, western blot analysis using antibodies for some apoptotic marker proteins such as caspase 3, p53, and Bax was performed. Cells can undergo apoptosis either by an extrinsic pathway, intrinsic pathway, or both. Activation of caspase 8 is responsible for the extrinsic pathway, while caspase 9 is responsible for the intrinsic pathway. However, both these pathways will ultimately activate caspase 3, which is the executioner caspase. The results (Figure 17) indicate that there is dose-dependent upregulation in the expression of the active form of caspase 3 as compared to the control. Cleavage of caspase 3 resulted in the active dimeric form of cleaved caspase 3 (17 and 19 kD) leading to apoptosis.⁵⁰ It can be observed that the expression level of p53 (tumor suppressor protein) increased⁵¹ drastically upon treatment with complex 1, which is possibly due to the activation of p53 occurring due to the observed DNA damage caused by complex 1. Also, it is known that p53 in particular interacts with Bax, a pro-apoptotic protein, stimulating its activation, and drugs that

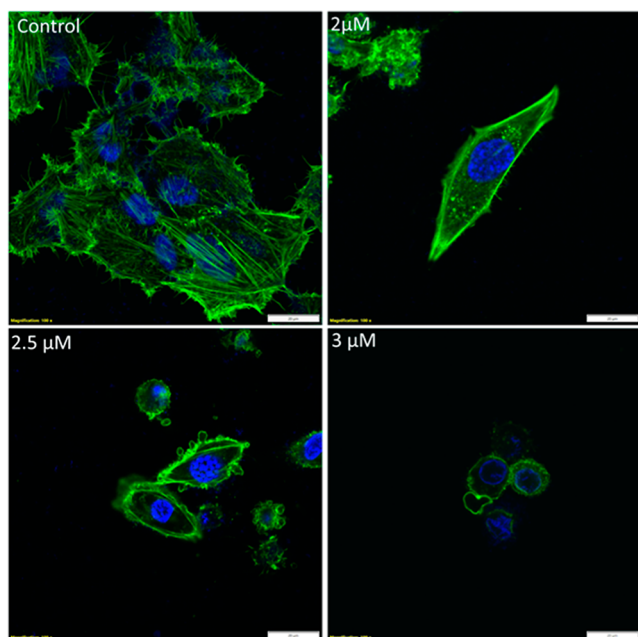


Figure 16. Cytoskeleton alterations for HeLa cells treated with varying amounts of **1** for 24 h. In control, green color actin filaments stained with phalloidin are clearly visible. Control has intact fibers (stained green) and an intact nucleus (stained blue with Hoechst 33342), whereas treated cells show damaged fibers, morphological alterations, and nuclear fragmentation.

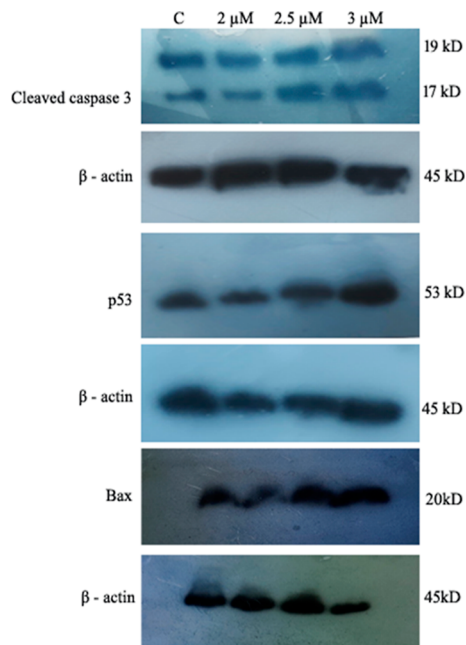


Figure 17. Protein expression of apoptotic markers such as caspase-3, p53, and bax determined by western blot analysis. β -Actin is used as a loading control for each.

activate Bax can serve as promising anticancer agents by inducing apoptosis in cancer cells.^{52,53} As observed in Figure 17, the expression of Bax was also seen to be upregulated upon treatment with complex **1**, further enhancing apoptosis in cancer cells. Thus, the results from western blot analysis showcase that complex **1** is responsible for pushing cancer cells toward apoptosis.

2.17. Cell Cycle Arrest Induced by Complex 1 in HeLa Cells. Flow cytometry was used to analyze the PI-stained cell population in different cell cycle stages.^{51,54} A typical cell cycle consists of four phases, that is, G1, S, G2, and M. Exposure of HeLa cells to complex **1** led to an increase in the cell population in the S phase, wherein DNA gets replicated. This population increase was prominent, and a dose-dependent increase with complex **1** concentration was observed. Control cells showed a 10.5% cell population in the S phase, which increased to 18.2% in the 3 μ M dose of complex **1** (Figure 18). Interestingly, at 2 μ M, both S phase and G2/M phase arrest was observed. This proves that complex **1** is a powerful tool against HeLa cervical cancer cells as it has been able to induce cell cycle arrest and hence prevent cancer cell proliferation. The result is also consistent with western blot results, where high p53 expression level was observed, as p53 is known to arrest cell cycle progression in case of DNA damage.

It is important to note here that the results observed for **1** may be compared to many other reported DNA-binding copper complexes.^{55–61} For example, the synthesized tyrosine Schiff base copper complexes by Reddy and Shilpa⁵⁵ showed good binding propensity for CT-DNA ($3.01\text{--}3.47 \times 10^4 \text{ M}^{-1}$) and exhibited high nuclease activity as evident from the high hydrolytic DNA-cleavage rate constant ($2.80\text{--}2.11 \text{ h}^{-1}$) that amounts to a significant rate enhancement (0.5 to 0.7×10^8 fold) in comparison to non-catalyzed DNA hydrolysis. Yu et al.⁵⁶ have reported four Cu(II) complexes of a reduced Schiff base ligand having diamine co-ligands that bind to DNA by intercalative mode and effectively induced apoptosis in cancer cells (A549, BGC823, and SGC7901), which was accompanied with increase in p53 and Bax and decrease in bcl2 expression. Hu et al.⁵⁷ have investigated the DNA/HSA binding ability and anticancer activity of three Cu(II) complexes having a quinolone-derived Schiff base ligand. The complexes interact with CT-DNA through intercalation mode and were found to significantly quench HSA fluorescence through a static quenching process. Cytotoxicity studies in the HeLa cell line revealed that their IC₅₀ values for 48 h ($9.98\text{--}18.72 \mu\text{M}$) were much lower than that of Cisplatin ($35.25 \mu\text{M}$). They were found to activate the bcl2 family of proteins and induce apoptosis via the ROS-mediated mitochondrial pathway. Rostas et al.⁵⁸ reported Cu(II) complexes of mixed heterocycle ligands that exhibited intercalative interaction with DNA and strong DNA-cleavage activity in the presence of ascorbate or H₂O₂. In vitro studies on B16 melanoma tumor cells (IC₅₀ at 48 h: $0.004\text{--}0.02 \text{ mM}$) indicated that the complexes have very high potential for development of antitumor agents.

3. CONCLUSIONS

A paramagnetic mononuclear mixed ligand copper(II) complex (**1**) containing an SNO-donor Schiff base ligand along with the heterocyclic *o*-phen co-ligand characterized using single-crystal X-ray crystallography was assessed for its interactions with DNA and HSA as well as its cytotoxicity toward HeLa cervical carcinoma cells and MDA-MB-231 human breast cancer cells. This compound binds to CT-DNA intercalatively as revealed from the UV–vis spectroscopic results, and that was further augmented by fluorescence spectroscopic results of the EB displacement experiment. Complex **1** was found to be highly efficient in conducting oxidative single-strand scission of pUC19 DNA and was also capable of cleaving DNA hydrolytically in the absence of any external agent or light ($k_{\text{obs}} = 1.987 \text{ h}^{-1}$). **1** showed a strong binding affinity with HSA, and a static

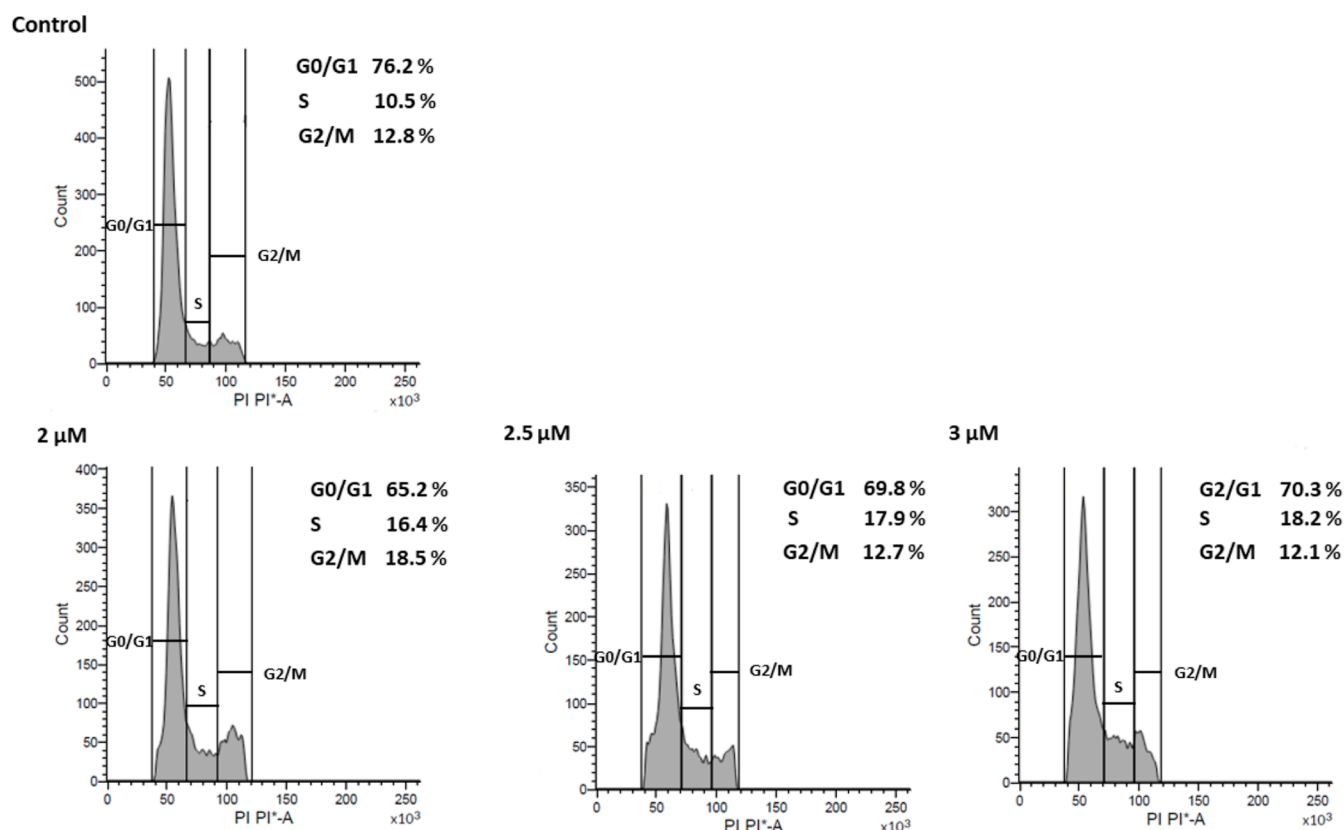


Figure 18. Effect of **1** on cell cycle progression: HeLa cells were treated with the indicated concentrations of **1** for 24 h, stained with PI, and the changes of cell cycle distribution were assessed by DNA flow cytometric analysis.

quenching mechanism was suggested for reduction of intrinsic fluorescence of HSA as reflected from the high k_q value ($2.29 \times 10^{13} \text{ M}^{-1} \text{ s}^{-1}$). FRET theory suggested close interaction between HSA (donor) and **1** (acceptor). Molecular docking studies suggested that **1** primarily binds to HSA in subdomain IIA, and the analyses of the docking results using the protein–ligand interaction profiler (PLIP) revealed the hydrophobic, hydrogen bonds, and π -cation interactions between HSA and the ligand. The compound exhibited significant cytotoxicity in HeLa as well as in MDA-MB-231 cancer cells as revealed from their IC_{50} values obtained from the MTT assay. Nuclear staining assays revealed that **1** induced apoptotic cell death in HeLa cells. Nuclear fragmentation and destruction of actin filaments were clearly observed from the effect of **1** on cytoskeletal actin filaments when visualized using fluorescein phalloidin and Hoechst as nuclear counterstain agents. Flow cytometric analysis suggested S phase cell cycle arrest in HeLa cells by **1**. A dose-dependent upregulation in the expressions of apoptotic marker proteins caspase 3, p53, and Bax was observed in the western blot analysis. These results collectively indicate that complex **1** induced apoptosis by promoting DNA damage and has high potential to act as an anticancer agent.

4. MATERIALS AND METHODS

4.1. Materials. *o*-Aminobenzenethiol and salicylaldehyde were purchased from Aldrich. Sodium dodecyl sulfate (SDS), Tris-base, glycine, sodium chloride, acrylamide/bis-acrylamide 30% solution, ammonium persulfate (APS), Bradford reagent, tetramethylethylenediamine (TEMED), SX Laemmli buffer, 2-mercaptoethanol, Poncheau-S stain, and a pre-stained protein marker were purchased from HiMedia. Tween 20 and a protease

inhibitor cocktail were purchased from Sigma. An immobilon-P polyvinylidene fluoride (PVDF) membrane with a 0.45 μm pore size was purchased from Merck Millipore. Antibodies, namely, anti-p53 (cat. no. 2527T), anti-caspase 3 (14220T), anti-beta actin (4970T), anti-bax (5053T), and goat horseradish peroxidase-linked anti-rabbit (7074P) were purchased from Cell Signaling Technology. The Clarity western enhanced chemiluminescence (ECL) substrate was purchased from Bio-Rad.

4.2. Syntheses. **4.2.1. Preparation of 2-(2-Hydroxyphenyl)benzthiazoline (A).** This compound was synthesized and characterized by following a method reported¹⁷ by us. Details of the preparation of this compound are presented in the [Supporting Information](#).

Anal. Calcd for $\text{C}_{13}\text{H}_{11}\text{NSO}$: C, 68.09; H, 4.84; N, 6.11. Found: C, 67.80; H, 4.78; N, 6.04%.

4.2.2. Preparation of the Complex $[\text{CuL}(\text{o-phen})]\cdot\text{H}_2\text{O}$ ($\text{H}_2\text{L} = \text{o-HOC}_6\text{H}_4\text{C}(\text{H})=\text{NC}_6\text{H}_4\text{SH-o}$). This was synthesized by modifying the method reported by Patel et al.¹⁶ A dark blue solution of $\text{Cu}(\text{OAc})_2\cdot\text{H}_2\text{O}$ (0.200 g, 0.001 mol) and 1,10-phenanthroline monohydrate (0.200 g, 0.001 mol) in methanol (20 mL) was added to a cream-colored methanol solution (25 mL) of 2-(2-hydroxyphenyl)benzthiazoline (**A**) (0.229 g, 0.001 mol) at room temperature (RT), and the dark-brown reaction mixture was stirred for 1 h. The brown solid that was separated from the solution was filtered, washed thoroughly with methanol, and dried. Yield $\sim 80\%$. Anal. Calcd for $\text{C}_{25}\text{H}_{19}\text{N}_3\text{O}_2\text{SCu}$: C, 61.40; H, 3.92; N, 8.60%. Found: C, 61.16; H, 3.89; N, 8.52%. ESI-MS (CH_3CN) m/z : 181.07 [*o*-phen + H]⁺; m/z 353.07 [$\text{Cu}_2(\text{C}_{13}\text{H}_8\text{NSO})^+$]; m/z 457.10 [(*o*-

HO-C₆H₄C(H)=N-C₆H₄-S-o)₂ + H⁺]. IR (KBr): $\nu(\text{C}\equiv\text{N})$ 1605 cm⁻¹.

Single crystals were grown from its acetonitrile solution at RT and used for determining its structure using X-ray crystallography.

4.3. X-ray Crystallography. A Bruker D8 VENTURE dual-source single-crystal X-ray diffractometer equipped with a PHOTON 100 detector was used for the data collection (Table 3). A Mo K α radiation source of wavelength 0.71073 Å was

Table 3. Crystal Parameters, Data Collection, and Structure Refinement for 1^a

empirical formula	C ₅₀ H ₃₆ Cu ₂ N ₆ O _{3.25} S ₂
formula weight	964.05
temperature	296(2) K
wavelength	0.71073 Å
crystal system	monoclinic
space group	C2/c
unit cell dimensions	$a = 31.0158(12)$ Å $\alpha = 90^\circ$ $b = 12.4944(5)$ Å $\beta = 100.4740(10)^\circ$ $c = 11.1773(4)$ Å $\gamma = 90^\circ$
volume	4259.3(3) Å ³
Z	4
density (calculated)	1.503 mg/m ³
absorption coefficient	1.150 mm ⁻¹
F(000)	1976
crystal size	0.150 × 0.150 × 0.100 mm ³
theta range for data collection	3.524 to 25.999°
index ranges	-38 ≤ h ≤ 38, -15 ≤ k ≤ 15, -13 ≤ l ≤ 13
reflections collected	36,234
independent reflections	4177 [R(int) = 0.0393]
completeness to $\theta = 25.242^\circ$	99.7%
absorption correction	semi-empirical from equivalents
max. and min. transmission	0.7456 and 0.6976
refinement method	full-matrix least-squares on F ²
data/restraints/parameters	4177/1/294
goodness-of-fit on F ²	1.021
final R indices [I > 2 σ (I)]	R ₁ = 0.0302, wR ₂ = 0.0721
R indices (all data)	R ₁ = 0.0447, wR ₂ = 0.0785
extinction coefficient	n/a
largest diff. peak and hole	0.248 and -0.300 e-Å ⁻³

^aThe CCDC number for 1 is 2164350.

selected for diffraction studies. A suitable single crystal of the size 0.1 × 0.15 × 0.15 mm³ was selected using a polarizing microscope, which was then mounted on a nylon loop with the help of Paraton-N oil. The crystal was then centered at the goniometer center with the aid of a video microscope. The automatic cell determination routine, with 36 frames (10 s exposure time/frame) at three different orientations of the detector, was employed to collect reflections for unit cell determination. The collected reflections were indexed using inbuilt Apex3 software to obtain unit cell parameters. An optimized strategy with fourfold redundancy per reflection was employed for the complete data collection. The collected data were integrated using the Bruker APEX-3/SAINT program.⁶² A multi-scan absorption correction was applied to the data using Bruker/SADABS.⁶² The structure was solved using a SHELXT-2014⁶³ and refined by full-matrix least-squares techniques using the SHELXL-2018⁶⁴ computer program. Molecular graphics were drawn using ORTEP3.⁶⁵ Aromatic hydrogens were fixed geometrically as a riding model at the calculated positions with

their $U_{\text{iso}}(\text{H}) = 1.2U_{\text{eq}}(\text{C})$. Hydrogen on water (O2) was located from different electron density peaks and refined freely, whereas hydrogen on O3 could not be located as it is only partially occupied at the twofold axis of rotation.

4.4. DNA Interaction. **4.4.1. Absorption Spectral Studies for DNA Binding.** The DNA binding experiment was carried out in 10 mM Tris-HCl buffer (pH = 7.43). To begin with, the concentration of CT-DNA was determined using absorption spectroscopy using the molar extinction coefficient at 260 nm as 6600 (mol L⁻¹)⁻¹ cm⁻¹. The CT-DNA solution displayed a ratio of UV absorbance at 260 nm and 280 nm of about 1.85, suggesting that the DNA was sufficiently free of protein impurities. Absorption titration experiments were conducted keeping constant the concentration of complex 1 (5×10^{-5} M) and varying the CT-DNA concentration from 0 to 12 μM . After addition of DNA to the solution of the copper complex, the resulting mixture was allowed to equilibrate at room temperature (25 °C), after which the spectra were recorded using a Jasco V-570 UV/VIS/NIR spectrophotometer. Thereafter, the spectral data were used to evaluate the intrinsic binding constant, which determines the binding ability of the complex to CT-DNA.

4.4.2. EB Fluorescence Displacement Experiment. In the EB fluorescence displacement experiment, 50 μM CT-DNA and 2 μM EB in 10 mM Tris-HCl buffer (pH = 8) solution were used. 1 was added to the EB-DNA solution in incremental amounts of 2.5 μM until saturation was observed at 42.5 μM . Prior to measurement, the mixture was incubated for 5 min. The fluorescence measurements were done using a Jasco spectrofluorometer FP-8500. The excitation wavelength λ_{ex} was 510 nm, and the emitted fluorescence was analyzed at 597 nm.

4.4.3. Viscosity Measurement. Viscosity measurement was carried using CT-DNA (100 μM) with increasing concentrations (0–100 μM) of complex 1 using an Ostwald viscometer. Viscosity values were calculated from the flow time of the buffer alone (t_0) and flow time of each sample (t) using the equation $\eta = (t - t_0)/t_0$. Data were presented by plotting values of relative viscosity (η/η_0)^{1/3} against [complex]/[DNA], where η is the viscosity of DNA in the presence of the complex and η_0 is the viscosity of the DNA alone.

4.5. DNA-Cleavage Experiment. To assess the DNA-cleavage ability of complex 1, pUC19 DNA (200 ng) was exposed to varying amounts of 1. To investigate the oxidative cleavage, the reaction mixture containing pUC19 DNA, Tris-HCl buffer (50 mM, pH 8), and complex 1 (0–4 μM) was treated with H₂O₂ (1 mM) and incubated for 2 h at 37 °C. To check the involvement of free radicals such as the hydroxyl radical and singlet oxygen in oxidative cleavage, scavengers such as DMSO (2 μL) and NaN₃ (500 μM) were also used, respectively. However, for hydrolytic cleavage, pUC19 DNA was exposed to different complex 1 concentrations (0–100 μM) for 2 h at 37 °C without the addition of any external reagent. Additionally, control experiments were included using ROS scavengers such as DMSO (2 μL) and NaN₃ (500 μM) to detect the presence of oxidants. Following the incubation, gel electrophoresis was carried out (for both hydrolytic and oxidative cleavage) in 1% agarose gel in 1× Tris acetic acid EDTA buffer, pH 8.4, for 1 h 30 min at 60 V. DNA was stained in 0.5 $\mu\text{g}/\text{mL}$ EB and visualized under UV light. The resulting bands were quantified using ImageJ software. The kinetics of hydrolytic DNA cleavage was studied to determine the cleavage rate. The experiment was conducted with 200 ng of pUC19 DNA and 200 μM complex 1 at 37 °C, and conversion of SC

DNA to NC DNA was observed with time. The data were fitted with a single exponential decay curve from which the hydrolysis rate constant k_{obs} was found, and then, an increase of the hydrolysis rate was also determined.

4.6. HSA Binding Studies. **4.6.1. Fluorescence Quenching Experiment.** Quenching measurements of HSA fluorescence were done using 4×10^{-6} M HSA in 20 mM sodium phosphate buffer at pH 7.4. The effect on the spectrum of the albumin solution was monitored by successive addition of complex **1** at an increment of $2 \mu\text{M}$. An experiment was performed at ambient temperature ($25 \text{ }^\circ\text{C}$), and the fluorescence emission spectra were scanned from 300 to 450 nm using an excitation wavelength of 295 nm.

4.6.2. UV–Vis Spectral Measurement. In the UV–vis absorption method, the concentrations of HSA and complex **1** were kept as $4 \mu\text{M}$, the absorption spectra were scanned in the 200–500 nm range, and the effect of complex **1** on the HSA spectrum was studied at ambient temperature ($25 \text{ }^\circ\text{C}$).

4.6.3. Synchronous and 3D Fluorescence Measurements. For synchronous fluorescence spectral experiments, the concentration of HSA was kept as $4 \mu\text{M}$, and to it, complex **1** was added in incremental amounts using 20 mM sodium phosphate buffer (pH = 7.4). The spectra were scanned at $\Delta\lambda = 15$ and 60 nm ($\Delta\lambda = \lambda_{\text{ex}} - \lambda_{\text{em}}$).

3D fluorescence of HSA was monitored in the absence and presence of complex **1** (molar ratio 1:1) and emission spectra recorded between 230 and 500 nm, starting with an initial excitation wavelength of 220 nm followed by an incremental increase by 10 nm up to 300 nm. Slit opening was kept as 5 nm.

4.7. FRET Measurement. Fluorescence energy transfer occurs due to the overlap of the spectrum of fluorophore (donor) and the absorption spectrum of the acceptor molecule. The fluorescence spectrum of HSA ($4 \mu\text{M}$) and the absorption spectrum of **1** ($4 \mu\text{M}$) were recorded. Overlap integral J and Förster distance r were determined from the plot of normalized emission intensity $\bar{I}_D(\lambda)$ of HSA and extinction coefficient $\epsilon_A(\lambda)$ of **1** in the 300–450 nm wavelength range.

4.8. Molecular Docking. Molecular docking simulation was performed using the AutoDock Vina Software^{66,67} to analyze the binding affinity of HSA with complex **1**. The crystal structure of the HSA molecule (PDB ID: 1H9Z) was accessed from Protein Data Bank (<http://www.rcsb.org/pdb/home/home.do>). Energy minimization calculation of the HSA molecule was performed using a GROMACS 3.0 molecular dynamics (MD) simulation package.^{68–70} Initially, the water molecules were removed, and hydrogen atoms were attached to the HSA structure during the energy minimization process. The entire MD simulation was conducted for 500,000 steps with a 0.002 fs timestep with the canonical (NVT) ensemble,⁷¹ keeping the volume and number of atoms fixed and using a modified Berendsen thermostat to maintain a constant temperature (300 K). The crystallographic information file (CIF) of **1** was obtained from X-ray diffraction data. Initially, the CIF file format was converted to pdbqt file format to continue the molecular docking simulation process. A grid box with the dimension of $94 \times 56 \times 96$ was considered with centers set at coordinates $x = 55.286$, $y = 56.552$, and $z = 57.497$ for the docking calculation. Autodock Vina was used for performing the local optimization calculation and achieving the lowest energy structure. In Autodock Vina, swarm optimization, genetic algorithms, and the Broyden–Fletcher–Goldfarb–Shanno (BFGS) algorithm are combined where the BFGS algorithm calculated the scoring function and its derivatives. 100 runs were performed to obtain

the most probable binding conformations and each run undergoes 20 iterations. The PyMOL software (The PyMOL Molecular Visualization System, Version 1.5, Schrodinger, LLC) was used to render the output structures. A PLIP⁴² was used to detect and visualize the interactions between the target protein molecule (HSA) and the ligand. Details of all interactions were listed on the atom level, enabling analyses of binding characteristics. PLIP detects hydrophobic interaction, hydrogen bonds, and π –cation interactions between a protein molecule and ligands via analyzing the docking results. The PLIP web server (<https://plip-tool.biotec.tu-dresden.de>) uses an interface where the PDB files of the final structures obtained from docking were used. PLIP performs four steps to calculate the relevant interactions: (i) preparation of the structure (the input structure is hydrogenated and the ligands are extracted along with their binding sites), (ii) functional characterization, (iii) rule-based matching, and (iv) filtering of interactions.

4.9. MTT Assay. Cell viability was determined by performing an MTT assay on both cancerous cell lines, namely, HeLa and MDA-MB-231. These cells were seeded in a 96-well plate with a density of 2×10^4 per well. These cells were allowed to attach overnight in a 5% CO_2 incubator, and then they were treated with varying amounts of **1**. Following 24 h of incubation with complex **1**, the cell viability was analyzed. Media were removed, and each well was subsequently stained with 0.5 mg/mL MTT dye for 4 h. After 4 h, the MTT dye was removed, and the resulting formazan crystals were dissolved in 100 μL of DMSO. Finally, absorbance reading was measured at 570 nm with the help of an enzyme-linked immunosorbent assay plate reader (Thermo Scientific Multiskan GO), and the cell viability percentage was determined from the absorbance reading. This was repeated with the free ligands using varying concentrations similar to those used for **1** to assess their cytotoxic effect on both the cell lines under similar experimental conditions.

4.10. Hoechst Staining. To visualize changes in the nuclei of cells under treatment, the cells were stained with Hoechst 33342. Briefly, 5×10^5 cells seeded in a 35 mm confocal dish were allowed to attach overnight and then exposed to treatment with **1**. One control dish was maintained without treatment. After 24 h of incubation with **1**, the cells were washed with $1 \times$ PBS, fixed with 4% paraformaldehyde, and permeabilized by adding 0.1% Triton X-100 in PBS for 10 min. Hoechst 33342 was used to stain the cells; then, they were kept in the dark for 15 min, rinsed with PBS three times, and finally examined using a fluorescence microscope.

4.11. AO/PI Dual Staining. Cellular morphology assessment was done using an AO and PI double staining assay.⁷² HeLa cells seeded in a 35 mm confocal dish with a density of 1×10^6 were placed in a CO_2 incubator overnight. The cells were then treated with three different complex **1** concentrations, and one dish was left untreated to be used as control. Upon 24 h of exposure to complex **1**, the cells were washed with $1 \times$ PBS and stained with AO ($40 \mu\text{M}$) and PI ($40 \mu\text{M}$) for 30 min at $37 \text{ }^\circ\text{C}$. Finally, these cells were washed with $1 \times$ PBS twice and viewed under a fluorescent microscope (OLYMPUS CKX53).

4.12. Staining of Actin Filaments. HeLa cells were seeded in a confocal dish with a density of 5×10^5 cells and were allowed to attach overnight in a humidified CO_2 incubator. They were treated with three different amounts of **1**. Untreated cells were used as control. Following a 24 h exposure to complex **1**, the actin filaments were stained with Phalloidin-iFluor 488 according to the manufacturer's protocol. Briefly, after the media were aspirated and washed in $1 \times$ PBS, cells were fixed

with 3% paraformaldehyde for 10 min and permeabilized with 0.1% Triton X 100 for 10 min. Finally, they were incubated in 400 μL per dish Phalloidin (1 $\mu\text{g}/\text{mL}$) for 30 min at room temperature along with Hoechst 33342. The cells were rinsed twice with 1 \times PBS and then visualized under a confocal microscope (OLYMPUS CKX53) at 100 \times .

4.13. Western Blotting. HeLa cells (1×10^6) were seeded in a 90 mm Petri dish. Upon attachment, these cells were treated with three different concentrations (2, 2.5, and 3 μM) of complex **1**. After 24 h, the cells were harvested and lysed with 100 μL of RIPA lysis buffer (HiMedia) along with a protease inhibitor, and protein was extracted by centrifugation at 14,000g for 15 min at 4 $^\circ\text{C}$, following which the protein concentration was determined using the Bradford reagent (HiMedia) and stored in -80°C until further use. For western blot analysis separation using SDS-PAGE, 60 μg of this protein was mixed with 5 \times Laemmli buffer and heated at 95 $^\circ\text{C}$ for 5 min. The sample protein was then separated using electrophoresis in a 12% SDS polyacrylamide gel at 70 V and then transferred onto a PVDF (Immobilon-P, Merck Millipore Ltd.) membrane using wet transfer. Protein bands were visualized by using Poncheau-S (HiMedia) and washed and blocked with 5% BSA in Tris-buffer and 0.1% Tween 20 for 1 h. Target proteins were probed overnight at 4 $^\circ\text{C}$ with rabbit anti-caspase 3 (1:1000, Cell Signaling Technology), rabbit anti-p53 (1:1000, Cell Signaling Technology), rabbit anti-bax (1:1000, Cell Signaling Technology), and rabbit anti-beta actin (1:1000, Cell Signaling Technology). In the case of p53, the membrane was stripped and reprobed with beta actin. Next, the membrane was washed in Tris buffer and 0.1% Tween 20 (TBS-T) 5 times for 5 min at room temperature. This was followed by 1 h of incubation at room temperature with horse-radish peroxidase-conjugated goat anti-rabbit secondary antibody (1:3000). Again, the membrane was washed in Tris-buffer and 0.1% Tween 20 (TBS-T) at room temperature to remove unbound antibodies. Finally, the membrane with the protein side up was exposed to ECL reagents (Bio-Rad Clarity Western ECL Substrate) in a dark room. The resultant chemiluminescence was detected using X-ray films. Images were taken of these X-ray films.

4.14. Cell Cycle Arrest. In order to investigate the cell population distribution within different stages of a cell cycle, flow cytometry was done. HeLa cells were seeded with a density of 5×10^5 cells per well in a six-well plate. Each concentration (control, 2, 2.5, and 3 μM) had three wells. These cells were allowed to adhere to the substrate overnight and then treated with three different amounts of **1**. After 24 h of incubation, cells were pooled by trypsinization and fixed with 70% ethanol for 30 min. To this, 10 μg of RNase was added in each sample. Finally, 50 $\mu\text{g}/\text{mL}$ PI was added to the samples and incubated for 30 min in ice in the dark. Samples were transferred to fluorescence-activated cell sorting (FACS) tubes and analyzed using BD FACS Melody. After appropriate gating of the cell population, distribution of the cell cycle was calculated.

Instrumental details for Physical Measurements are given in the Supporting Information.

■ ASSOCIATED CONTENT

SI Supporting Information

The Supporting Information is available free of charge at <https://pubs.acs.org/doi/10.1021/acsomega.2c02354>.

ESI-MS spectrum of **1** in CH_3CN ; IR spectrum of 2-(2-hydroxyphenyl)-benzthiazoline and **1**; electronic spec-

trum of **1**; X-band EPR spectra of **1**; MTT assay of the free ligands with the cancer cell lines HeLa and MDA-MB-231; and Hoechst staining showing typical apoptotic morphological changes after treatment of HeLa cells with complex **1** (PDF)

CCDC number is 2164350 for compound **1**. These data can be obtained free of charge via <http://www.ccdc.cam.ac.uk/conts/retrieving.html>, or from the Cambridge Crystallographic Data Centre, 12 Union Road, Cambridge CB2 1EZ, UK; Fax: (+044) 1223-336-033; or E-mail: deposit@ccdc.cam.ac.uk Crystallographic information of **1** (CIF)

■ AUTHOR INFORMATION

Corresponding Author

Manjuri Kumar – Department of Chemical Engineering, Birla Institute of Technology and Science-Pilani, Zuarinagar, Goa 403726, India; orcid.org/0000-0002-8102-8923; Email: manjuri@goa.bits-pilani.ac.in

Authors

Kumudini Paliwal – Department of Chemical Engineering, Birla Institute of Technology and Science-Pilani, Zuarinagar, Goa 403726, India

Paramita Haldar – Department of Chemical Engineering, Birla Institute of Technology and Science-Pilani, Zuarinagar, Goa 403726, India

P. K. Sudhadevi Antharjanam – Sophisticated Analytical Instrument Facility, Indian Institute of Technology-Madras, Chennai 600 036, India; orcid.org/0000-0002-8801-7530

Complete contact information is available at:

<https://pubs.acs.org/10.1021/acsomega.2c02354>

Notes

The authors declare no competing financial interest.

■ ACKNOWLEDGMENTS

M.K. thanks SERB, Department of Science and Technology (DST), New Delhi, Govt. of India, for the project EMR/2017/001562. The authors thank SAIF, IIT-Madras for XRD; SAIF, IIT-Bombay for EPR spectra; and the CSIR-National Chemical Laboratory (NCL), Pune for high-resolution mass spectrum of the compound. Facilities provided by the Department of Biological Sciences and the CSIF of our Institute are gratefully acknowledged.

■ REFERENCES

- (1) Jamieson, E. R.; Lippard, S. J. Structure, recognition, and processing of cisplatin-DNA adducts. *Chem. Rev.* **1999**, *99*, 2467–2498.
- (2) Hambley, T. W. Developing new metal-based therapeutics: challenges and opportunities. *Dalton Trans.* **2007**, *43*, 4929–4937.
- (3) Amin, A.; Buratovich, M. New Platinum and Ruthenium complexes—the latest class of potential chemotherapeutic drugs—a review of recent developments in the field. *Mini-Rev. Med. Chem.* **2009**, *9*, 1489–1503.
- (4) Barone, G.; Terenzi, A.; Lauria, A.; Almerico, A. M.; Leal, J. M.; Busto, N.; García, B. DNA-binding of nickel (II), copper (II) and zinc (II) complexes: Structure–affinity relationships. *Coord. Chem. Rev.* **2013**, *257*, 2848–2862.
- (5) Johnstone, T. C.; Park, G. Y.; Lippard, S. J. Understanding and improving platinum anticancer drugs – phenanthriplatin. *Anticancer Res.* **2014**, *34*, 471–476.

- (6) Johnstone, T. C.; Suntharalingam, K.; Lippard, S. J. The next generation of platinum drugs: Targeted Pt(II) agents, nanoparticle delivery, and Pt(IV) prodrugs. *Chem. Rev.* **2016**, *116*, 3436–3486.
- (7) Ott, I.; Gust, R. Non platinum metal complexes as anti-cancer drugs. *Arch. Pharm.* **2007**, *340*, 117–126.
- (8) Santini, C.; Pellei, M.; Gandin, V.; Porchia, M.; Tisato, F.; Marzano, C. Advances in copper complexes as anticancer agents. *Chem. Rev.* **2014**, *114*, 815–862.
- (9) Hazra, M.; Dolai, T.; Pandey, A.; Dey, S. K.; Patra, A. Synthesis and characterisation of copper (II) complexes with tridentate NNO functionalized ligand: Density function theory study, DNA binding mechanism, optical properties, and biological application. *Bioinorg. Chem. Appl.* **2014**, *2014*, 104046.
- (10) More, M. S.; Joshi, P. G.; Mishra, Y. K.; Khanna, P. K. Metal complexes driven from Schiff bases and semicarbazones for biomedical and allied applications: a review. *Mater. Today Chem.* **2019**, *14*, 100195.
- (11) Bashkin, J. K. Introduction to RNA/DNA cleavage. *Chem. Rev.* **1998**, *98*, 937–938.
- (12) Dhar, S.; Reddy, P. A. N.; Chakravarty, A. R. Intramolecular nucleophilic activation promoting efficient hydrolytic cleavage of DNA by (aqua) bis (dipyridoquinoxaline) copper (II) complex. *Dalton Trans.* **2004**, *5*, 697–698.
- (13) Lu, J.; Sun, Q.; Li, J.-L.; Jiang, L.; Gu, W.; Liu, X.; Tian, J.-L.; Yan, S.-P. Two water-soluble copper (II) complexes: synthesis, characterization, DNA cleavage, protein binding activities and in vitro anticancer activity studies. *J. Inorg. Biochem.* **2014**, *137*, 46–56.
- (14) Shen, F.; Liu, Y.-X.; Li, S.-M.; Jiang, C.-K.; Wang, B.-F.; Xiong, Y.-H.; Mao, Z.-W.; Le, X.-Y. Synthesis, crystal structures, molecular docking and in vitro cytotoxicity studies of two new copper(II) complexes: special emphasis on their binding to HSA. *New J. Chem.* **2017**, *41*, 12429–12441.
- (15) Hoogenboezem, E. N.; Duvall, C. L. Harnessing albumin as a carrier for cancer therapies. *Adv. Drug Delivery Rev.* **2018**, *130*, 73–89.
- (16) Patel, R. N.; Gundla, V. L. N.; Patel, D. K. Synthesis, characterization and properties of some ternary copper(II) complexes containing NOS donor Schiff base and NN donor bidentate ligands. *Indian J. Chem.* **2008**, *47*, 353–360.
- (17) Koley, M. K.; Sivasubramanian, S. C.; Varghese, B.; Manoharan, P. T.; Koley, A. P. Synthesis and characterization of two stable paramagnetic octahedral chromium(IV) complexes with dianionic tridentate SNO donor ligands and of a chromium(III) complex with a ONO donor ligand. *Inorg. Chim. Acta* **2008**, *361*, 1485–1495.
- (18) Addison, A. W.; Rao, T. N.; Reedijk, J.; van Rijn, J.; Verschoor, G. C. Synthesis, structure, and spectroscopic properties of copper(II) compounds containing nitrogen–sulphur donor ligands; the crystal and molecular structure of aqua[1,7-bis(N-methylbenzimidazol-2'-yl)-2,6-dithiaheptane]copper(II) perchlorate. *J. Chem. Soc., Dalton Trans.* **1984**, *7*, 1349–1356.
- (19) Erxleben, A. Investigation of non-covalent interactions of metal complexes with DNA in cell-free systems. *Chimia* **2017**, *71*, 102–111.
- (20) Sissi, C.; Mancin, F.; Gatos, M.; Palumbo, M.; Tecilla, P.; Tonellato, U. Efficient plasmid DNA cleavage by a mononuclear copper (II) complex. *Inorg. Chem.* **2005**, *44*, 2310–2317.
- (21) Rabindra Reddy, P.; Shilpa, A. Synthesis, characterization, and DNA-binding and cleavage properties of dinuclear Cu^{II}-Salophen/Salen complexes. *Chem. Biodiversity* **2011**, *8*, 1245–1265.
- (22) Chen, S.; Lai, W.; Li, X.; Wang, H. Necrosulfonamide selectively induces DNA double-strand breaks in acute myeloid leukemia cells. *Chem. Res. Toxicol.* **2022**, *35*, 387–391.
- (23) Dedon, P. C. The chemical toxicology of 2-deoxyribose oxidation in DNA. *Chem. Res. Toxicol.* **2008**, *21*, 206–219.
- (24) Dedon, P. C.; Goldberg, I. H. Free-radical mechanisms involved in the formation of sequence-dependent bistranded DNA lesions by the antitumor antibiotics bleomycin, neocarzinostatin, and calicheamicin. *Chem. Res. Toxicol.* **1992**, *5*, 311–332.
- (25) Burstyn, J. N.; Deal, K. A. Selective catalytic hydrolysis of a simple phosphodiester by a macrocyclic copper (II) complex. *Inorg. Chem.* **1993**, *32*, 3585–3586.
- (26) Dhar, S.; Reddy, P. A. N.; Chakravarty, A. R. Intramolecular nucleophilic activation promoting efficient hydrolytic cleavage of DNA by (aqua)bis-(dipyridoquinoxaline)copper(II) complex. *Dalton Trans.* **2004**, 697–698.
- (27) Uma, V.; Kanthimathi, M.; Weyhermuller, T.; Nair, B. U. Oxidative DNA cleavage mediated by a new copper (II) terpyridine complex: Crystal structure and DNA binding studies. *J. Inorg. Biochem.* **2005**, *99*, 2299–2307.
- (28) Anbu, S.; Shanmugaraju, S.; Kandaswamy, M. Electrochemical, phosphate hydrolysis, DNA binding and DNA cleavage properties of new polyaza macrobicyclic dinickel (II) complexes. *RSC Adv.* **2012**, *2*, 5349–5357.
- (29) Daniels, J. S.; Gates, K. S. DNA Cleavage by the antitumor agent 3-amino-1,2,4-benzotriazine 1,4-dioxide (SR4233): evidence for involvement of hydroxyl radical. *J. Am. Chem. Soc.* **1996**, *118*, 3380–3385.
- (30) Deal, K. A.; Hengge, A. C.; Burstyn, J. N. Characterization of transition states in dichloro (1,4,7-triazacyclononane) copper (II)-catalyzed activated phosphate diester hydrolysis. *J. Am. Chem. Soc.* **1996**, *118*, 1713–1718.
- (31) Reddy, P. A. N.; Nethaji, M.; Chakravarty, A. R. Hydrolytic cleavage of DNA by ternary amino acid Schiff base copper (II) complexes having planar heterocyclic ligands. *Eur. J. Inorg. Chem.* **2004**, 1440–1446.
- (32) Li, F.-z.; Xie, J.-q.; Feng, F.-m. Copper and zinc complexes of a diaza-crown ether as artificial nucleases for the efficient hydrolytic cleavage of DNA. *New J. Chem.* **2015**, *39*, 5654–5660.
- (33) Parsekar, S. U.; Fernandes, J.; Banerjee, A.; Chouhan, O. P.; Biswas, S.; Singh, M.; Mishra, D. P.; Kumar, M. DNA binding, cleavage and cytotoxicity studies of three mononuclear Cu(II) chloro-complexes containing N–S donor Schiff base ligands. *J. Biol. Inorg. Chem.* **2018**, *23*, 1331–1349.
- (34) Shen, F.; Ou, Z.-B.; Liu, Y.-J.; Liu, W.; Wang, B.-F.; Mao, Z.-W.; Le, X.-Y. Two Cu(II) complexes containing 2,4-diamino-6-(2-pyridyl)-1,3,5-triazine and amino acids: Synthesis, crystal structures, DNA/HSA binding, molecular docking, and in vitro cytotoxicity studies. *Inorg. Chim. Acta* **2017**, *465*, 1–13.
- (35) Munteanu, A.-C.; Badea, M.; Olar, R.; Silvestro, L.; Mihaila, M.; Brasoveanu, L. I.; Musat, M. G.; Andries, A.; Uivarosi, V. Cytotoxicity studies, DNA interaction and protein binding of new Al (III), Ga (III) and In (III) complexes with 5-hydroxyflavone. *Appl. Organomet. Chem.* **2018**, *32*, No. e4579.
- (36) Zhang, J.; Gao, X.; Huang, J.; Wang, H. Probing the interaction between human serum albumin and 9-hydroxyphenanthrene: A spectroscopic and molecular docking study. *ACS Omega* **2020**, *5*, 16833–16840.
- (37) Tabassum, S.; Al-Asbahy, W. M.; Afzal, M.; Arjmand, F.; Hasan Khan, R. Interaction and photo-induced cleavage studies of a copper based chemotherapeutic drug with human serum albumin: spectroscopic and molecular docking study. *Mol. Biosyst.* **2012**, *8*, 2424–2433.
- (38) Rahman, S.; Rehman, M. T.; Rabbani, G.; Khan, P.; AlAjmi, M. F.; Hassan, M. I.; Muteeb, G.; Kim, J. Insight of the interaction between 2,4-thiazolidinedione and human serum albumin: A spectroscopic, thermodynamic and molecular docking study. *Int. J. Mol. Sci.* **2019**, *20*, 2727.
- (39) Hussain, A.; AlAjmi, M. F.; Rehman, M. T.; Amir, S.; Husain, F. M.; Alsalmeh, A.; Siddiqui, M. A.; AlKhedhairi, A. A.; Khan, R. A. Copper (II) complexes as potential anticancer and Nonsteroidal anti-inflammatory agents: In vitro and in vivo studies. *Sci. Rep.* **2019**, *9*, 5237.
- (40) *FRET-Förster Resonance Energy Transfer: From Theory to Applications*; Medintz, I. L., Hildebrandt, N., Eds.; John Wiley & Sons, 2013.
- (41) Sudlow, G.; Birkett, D. J.; Wade, D. N. The characterization of two specific drug binding sites on human serum albumin. *Mol. Pharmacol.* **1975**, *11*, 824–832.
- (42) Adasme, M. F.; Linnemann, K. L.; Bolz, S. N.; Kaiser, F.; Salentin, S.; Haupt, V. J.; Schroeder, M. PLIP 2021: expanding the scope of the protein–ligand interaction profiler to DNA and RNA. *Nucleic Acids Res.* **2021**, *49*, W530–W534.

- (43) Rajendiran, V.; Karthik, R.; Palaniandavar, M.; Stoeckli-Evans, H.; Periasamy, V. S.; Akbarsha, M. A.; Srinag, B. S.; Krishnamurthy, H. Mixed-ligand copper (II)-phenolate complexes: effect of coligand on enhanced DNA and protein binding, DNA cleavage, and anticancer activity. *Inorg. Chem.* **2007**, *46*, 8208–8221.
- (44) Saswati, S.; Chakraborty, A.; Dash, S. P.; Panda, A. K.; Acharyya, R.; Biswas, A.; Mukhopadhyay, S.; Bhutia, S. K.; Crochet, A.; Patil, Y. P.; Nethaji, M.; Dinda, R. Synthesis, X-ray structure and in vitro cytotoxicity studies of Cu(i/ii) complexes of thiosemicarbazone: special emphasis on their interactions with DNA. *Dalton Trans.* **2015**, *44*, 6140–6157.
- (45) Zahedifard, M.; Lafta Faraj, F.; Paydar, M.; Yeng Looi, C.; Hajrezaei, M.; Hasanpourghadi, M.; Kamalidehghan, B.; Abdul Majid, N.; Mohd Ali, H.; Ameen Abdulla, M. Synthesis, characterization and apoptotic activity of quinazolinone Schiff base derivatives toward MCF-7 cells via intrinsic and extrinsic apoptosis pathways. *Sci. Rep.* **2015**, *5*, 11544.
- (46) Hajrezaei, M.; Paydar, M.; Zorofchian Moghadamtousi, S.; Hassandarvish, P.; Gwaram, N. S.; Zahedifard, M.; Rouhollahi, E.; Karimian, H.; Looi, C. Y.; Ali, H. M.; Abdul Majid, N.; Abdulla, M. A. A Schiff base-derived copper (II) complex is a potent inducer of apoptosis in colon cancer cells by activating the intrinsic pathway. *Sci. World J.* **2014**, *2014*, 540463.
- (47) Desouza, M.; Gunning, P. W.; Stehn, J. R. The actin cytoskeleton as a sensor and mediator of apoptosis. *Bioarchitecture* **2012**, *2*, 75–87.
- (48) Koňariková, K.; Perdikaris, G. A.; Gbelcova, H.; Andrezálová, L.; Švéda, M.; Ruml, T.; Laubertová, L.; Žitňanová, I. Effect of Schiff base Cu (II) complexes on signaling pathways in HT-29 cells. *Mol. Med. Rep.* **2016**, *14*, 4436–4444.
- (49) Povea-Cabello, S.; Oropesa-Ávila, M.; de la Cruz-Ojeda, P.; Villanueva-Paz, M.; De la Mata, M.; Suárez-Rivero, J.; Álvarez-Córdoba, M.; Villalón-García, I.; Cotán, D.; Ybot-González, P.; Sánchez-Alcázar, J. Dynamic reorganization of the cytoskeleton during apoptosis: the two coffins hypothesis. *Int. J. Mol. Sci.* **2017**, *18*, 2393.
- (50) Kuo, H.-M.; Tseng, C.-C.; Chen, N.-F.; Tai, M.-H.; Hung, H.-C.; Feng, C.-W.; Cheng, S.-Y.; Huang, S.-Y.; Jean, Y.-H.; Wen, Z.-H. MSP-4, an antimicrobial peptide, induces apoptosis via activation of extrinsic Fas/FasL-and intrinsic mitochondria-mediated pathways in one osteosarcoma cell line. *Mar. Drugs* **2018**, *16*, 8.
- (51) Parsekar, S. U.; Velankanni, P.; Sridhar, S.; Haldar, P.; Mate, N. A.; Banerjee, A.; Sudhadevi Antharjanam, P. K.; Koley, A. P.; Kumar, M. Protein binding studies with human serum albumin, molecular docking and in vitro cytotoxicity studies using HeLa cervical carcinoma cells of Cu(II)/Zn(II) complexes containing a carbohydrazone ligand. *Dalton Trans.* **2020**, *49*, 2947–2965.
- (52) Miyashita, T.; Krajewski, S.; Krajewska, M.; Wang, H. G.; Lin, H. K.; Liebermann, D. A.; Hoffman, B.; Reed, J. C. Tumor suppressor p53 is a regulator of bcl-2 and bax gene expression in vitro and in vivo. *Oncogene* **1994**, *9*, 1799–1805.
- (53) Westphal, D.; Kluck, R. M.; Dewson, G. Building blocks of the apoptotic pore: how Bax and Bak are activated and oligomerize during apoptosis. *Cell Death Differ.* **2014**, *21*, 196–205.
- (54) Parsekar, S. U.; Paliwal, K.; Haldar, P.; Antharjanam, P. K. S.; Kumar, M. Synthesis, characterization, crystal structure, DNA and HSA interactions as well as anticancer activity of a mononuclear Cu(II) complex with a Schiff base ligand containing a thiadiazoline moiety. *ACS Omega* **2022**, *7*, 2881–2896.
- (55) Reddy, P. R.; Shilpa, A. Oxidative and hydrolytic DNA cleavage by Cu (II) complexes of salicylidene tyrosine schiff base and 1, 10 phenanthroline/bipyridine. *Polyhedron* **2011**, *30*, 565–572.
- (56) Yu, H.; Yang, Y.; Li, Q.; Ma, T.; Xu, J.; Zhu, T.; Xie, J.; Zhu, W.; Cao, Z.; Dong, K.; Huang, J.; Jia, L. Ternary dinuclear copper (II) complexes of a reduced schiff base ligand with diimine coligands: DNA binding, cytotoxic cell apoptosis, and apoptotic mechanism. *Chem. Biol. Drug Des.* **2016**, *87*, 398–408.
- (57) Hu, K.; Liu, C.; Li, J.; Liang, F. Copper (II) complexes based on quinoline-derived Schiff-base ligands: synthesis, characterization, HSA/DNA binding ability, and anticancer activity. *MedChemComm* **2018**, *9*, 1663–1672.
- (58) Rostas, A. M.; Badea, M.; Ruta, L. L.; Farcasanu, I. C.; Maxim, C.; Chifriuc, M. C.; Popa, M.; Luca, M.; Celan Korosin, N.; Cerc Korosec, R.; Bacalun, M.; Raileanu, M.; Olar, R. Copper(II) complexes with mixed heterocycle ligands as promising antibacterial and antitumor species. *Molecules* **2020**, *25*, 3777.
- (59) Dhar, S.; Senapati, D.; Das, P. K.; Chattopadhyay, P.; Nethaji, M.; Chakravarty, A. R. Ternary copper complexes for photocleavage of DNA by red light: direct evidence for sulfur-to-copper charge transfer and d–d band involvement. *J. Am. Chem. Soc.* **2003**, *125*, 12118–12124.
- (60) Indoria, S.; Sood, H.; AroraRandhawa, D. S. B. S.; Garcia-Santos, I.; Smolinski, V. A.; Jasinski, J. P. Synthesis of 5-nitro-salicylaldehyde-N-substituted thiosemicarbazones of copper(II): molecular structures, spectroscopy, ESI-mass studies and antimicrobial activity. *Inorg. Chim. Acta* **2017**, *461*, 248–260.
- (61) Shanmugaiah, M. K.; Mekkandi Palsamy, K.; Lokesh, R.; N, I. G.; Mitu, L.; Jegathalaprathaban, R.; Gurusamy, R. Ternary copper (II) complex based chemical probes for DNA targeting: cytotoxic activity under visible light. *Appl. Organomet. Chem.* **2019**, *33*, No. e4762.
- (62) Bruker. Apex3, v2017.3.0, SAINT V8.38A; Bruker AXS Inc.: Madison (WI), USA, 2016, 2013/2014.
- (63) Sheldrick, G. M. SHELXL, version 2014; University of Göttingen: Germany, 2014.
- (64) Sheldrick, G. M. SHELXL-2018; University of Göttingen: Germany, 2018.
- (65) Fruglia, L. J. ORTEP-3 for Windows - a version of ORTEP-III with a Graphical User Interface (GUI). *J. Appl. Crystallogr.* **1997**, *30*, 565.
- (66) Eberhardt, J.; Santos-Martins, D.; Tillack, A. F.; Forli, S. AutoDock Vina 1.2.0: New docking methods, expanded force field, and python bindings. *J. Chem. Inf. Model.* **2021**, *61*, 3891–3898.
- (67) Trott, O.; Olson, A. J. AutoDock Vina: improving the speed and accuracy of docking with a new scoring function, efficient optimization, and multithreading. *J. Comput. Chem.* **2010**, *31*, 455–461.
- (68) Bekker, H.; Berendsen, H. J. C.; Dijkstra, E. J.; Achterop, S.; van Drunen, R.; van der Spoel, D.; Sijbers, A.; Keegstra, H. Gromacs: A parallel computer for molecular dynamics simulations. *Phys. Comput.* **1993**, *92*, 252–256.
- (69) Berendsen, H. J. C.; van der Spoel, D.; van Drunen, R. GROMACS: A message-passing parallel molecular dynamics implementation. *Comput. Phys. Commun.* **1995**, *91*, 43–56.
- (70) Lindahl, E.; Hess, B.; van der Spoel, D. GROMACS 3.0: A package for molecular simulation and trajectory analysis. *J. Mol. Model.* **2001**, *7*, 306–317.
- (71) Allen, M. P.; Tildesley, D. J. *Computer Simulation of Liquids*; Clarendon Press, 1987.
- (72) Parsekar, S. U.; Haldar, P.; Sudhadevi Antharjanam, P. K.; Kumar, M.; Koley, A. P. Synthesis, characterization, crystal structure, DNA and human serum albumin interactions, as well as antiproliferative activity of a Cu(II) complex containing a Schiff base ligand formed in situ from the Cu(II)-induced cyclization of 1,5-bis(salicylidene)-thiocarbohydrazone. *Appl. Organomet. Chem.* **2021**, *35*, No. e6152.